

DYNAMICAL STUDIES OF MISALIGNED CIRCUMBINARY DISKS

By

Ian C. Rabago

Bachelor of Science - Physics
Bachelor of Science - Mathematics
University of Nevada, Las Vegas
2018

Master of Science - Astronomy
University of Nevada, Las Vegas
2020

A dissertation submitted in partial fulfillment
of the requirements for the

Doctor of Philosophy – Astronomy

Department of Physics and Astronomy
College of Sciences
The Graduate College

University of Nevada, Las Vegas
May 2024



Dissertation Approval

The Graduate College
The University of Nevada, Las Vegas

April 3, 2024

This dissertation prepared by

Ian C. Rabago

entitled

Dynamical Studies of Misaligned Circumbinary Disks

is approved in partial fulfillment of the requirements for the degree of

Doctor of Philosophy – Astronomy
Department of Physics and Astronomy

Zhaohuan Zhu, Ph.D.
Examination Committee Chair

Jason Steffen, Ph.D.
Examination Committee Member

Rebecca Martin, Ph.D.
Examination Committee Member

Arya Udry, Ph.D.
Graduate College Faculty Representative

Alyssa Crittenden, Ph.D.
*Vice Provost for Graduate Education &
Dean of the Graduate College*

ABSTRACT

DYNAMICAL STUDIES OF MISALIGNED CIRCUMBINARY DISKS

by

Ian C. Rabago

Zhaohuan Zhu, Examination Committee Chair
Professor of Physics and Astronomy
University of Nevada, Las Vegas

Binary stars are common outcomes of the star formation process, with nearly half of Sun-like stars forming as part of a binary pair. The presence of a second star adds additional complexity and dynamical effects to the planet formation process in the surrounding circumbinary disk. In this work, I investigate the behavior of a circumbinary disk using hydrodynamic modeling, specifically in the case where the disk is misaligned to the binary orbital plane. Around eccentric binaries, highly inclined disks can align themselves perpendicular to the binary orbital plane. These “polar disks” can produce vortices and spiral arms when the disk viscosity is low. These vortices may accelerate the formation of polar-aligned circumbinary planets. Precession induced from the binary can distort the disk and cause it to warp in three-dimensional space. I examine the behavior of disk warping around a central binary using both analytic and numerical methods, deriving a new criterion for disk breaking. These criteria show consistency with both simulations and observed disks.

ACKNOWLEDGEMENTS

This work was supported in part by funding from the Nevada NASA Space Grant Consortium. The simulations shown in this work were conducted using the NASA High-End Computing (HEC) Program through the NASA Advanced Supercomputing (NAS) Division at Ames Research Center. Figures in this work were created with the help of NUMPY (Harris et al. 2020), MATPLOTLIB (Hunter 2007), and VISIT (Childs et al. 2012), as well the NAS Visualization Team.

Thank you to my advisor, Dr. Zhaohuan Zhu, for providing guidance through this whole project. Additional thanks to the UNLV Physics and Astronomy Graduate Department, for transforming this place into a more lively location over the years.

As before, I want to thank the teachers I have learned from on the way to this point. Without all of you I would not be here. And thank you to my friends and family, for your endless support throughout the years.

TABLE OF CONTENTS

ABSTRACT	iii
ACKNOWLEDGEMENTS	iv
LIST OF TABLES	vii
LIST OF FIGURES	xi
CHAPTER 1 INTRODUCTION: MISALIGNED DISKS IN THE UNIVERSE	1
CHAPTER 2 TIMESCALES OF DISK EVOLUTION	8
2.1 Disk Breaking in the Wave-like Regime	10
2.2 A Criterion for Viscous Disk Breaking	14
2.3 An Application to GW Orionis	15
2.4 Multiple Disk Breaking	19
CHAPTER 3 METHODS	22
3.1 Polar-Aligning Disks	25
3.2 Polar-Aligning Warped Disks	28
3.3 GW Orionis	29
3.4 Multiple Breaks	30
CHAPTER 4 VORTEX FORMATION IN POLAR DISKS	32
4.1 Polar Alignment of the Disk	32
4.2 Formation of Anticyclonic Vortices in Low-Viscosity Disks	38
CHAPTER 5 WARPS AND BREAKS IN CIRCUMBINARY DISKS	45
5.1 Warping and Breaking in Polar Disks	45
5.2 GW Orionis	53
5.3 Multiple Disk Breaking	54
CHAPTER 6 DISCUSSION	59
6.1 The effect of vortices vs. lumps in the disk	59
6.2 Viscosity in Warped Disks	63
6.3 Efficacy of the Disk Breaking Equations	64
6.4 Observational Signatures of Warped Disks	68
6.5 Prospects for Circumbinary Planets	71
CHAPTER 7 CONCLUSIONS	74
APPENDIX	77
BIBLIOGRAPHY	81

CURRICULUM VITAE 91

LIST OF TABLES

3.1	Table of parameters used in the simulations. Parameters are sorted in groups of binary arrangement (top), disc geometry (middle), and disk structure (bottom).....	25
-----	--	----

LIST OF FIGURES

2.1	Disk timescales t_p and t_c as a function of disk radius on a logarithmic scale. The red vertical line indicates the expected location of a disk breaking event based on Equations (2.11) and (2.12). For this figure, we consider a nearly coplanar disk around an equal mass binary with $e_b = 0.5$, extending from $r_{\text{in}} = 2a_b$ to $r_{\text{out}} = 50a_b$. The disk has a constant scale height $h/r = 0.1$, with power law slopes of $p = 1.5$ and $s = 1.0$	9
2.2	Predicted disk evolution of the Kraus et al. (2020) parameters, as inferred from our timescale equations. In each panel the lines are the same as Fig. 2.1. The shaded region indicates the inner cavity of the disk. <i>Top</i> : Early on, the inner edge of the disk is far enough out that a break does not occur. <i>Middle</i> : As the disk evolves, the inner edge drifts inwards until $r_{\text{in}} = 21.25$ au, where a break spontaneously occurs at 49 au. <i>Bottom</i> : As the inner edge continues to drift inwards, so does the expected breaking radius. Once the inner disk reaches an inner radius of 20 au, the expected breaking radius has moved to a radius of roughly 35 au.	17
2.3	Predicted number of breaks for a disk with a given initial geometry, shown as a function of the surface density and temperature power-law exponents p and s . The radial extent of the disk is given as $r_{\text{disk}} = [r_{\text{in}}, r_{\text{out}}]$ and the initial scale height is given at a distance of $r = 5a_b$. The central binary is an equal mass binary with eccentricity $e_b = 0.5$. <i>Left</i> : Initial inner radius and scale height. <i>Middle</i> : Effect of a larger inner disk radius. <i>Right</i> : Effect of a larger disk aspect ratio. The ‘×’ in each panel marks the disk parameters used in our multiple break simulation (Section 3.4)	20
3.1	Example of the inclined disk simulation setup.	23
3.2	Schematic of the central binary and circumbinary disk arrangement used for polar disk simulations, as well as the angles used to measure the disk orientation. The binary orbits in the xz-plane, with the angular momentum vector L_b pointing along the positive y-axis and the eccentricity vector e_b pointing along the z-axis. The disk is oriented in 3D space by its angular momentum vector L_{disk} , where it forms an angle i with the vector L_b . The gray dashed line denotes the disk’s “line of nodes”, where the disk crosses the xz-plane at an angle Ω with the vector e_b as a reference direction.	27
4.1	Time evolution of the disk for different values of α , showing large changes in orientation. <i>Top</i> : Disk inclination i . <i>Top Middle</i> : Longitude of ascending node Ω . <i>Middle</i> : Angle between the disk and the binary eccentricity vector θ_{polar} . <i>Bottom Middle</i> : Longitude of ascending node in the xy-plane Ω_{polar} . <i>Bottom</i> : Disk mass as a fraction of the initial mass. All angular quantities are measured in reference to the binary orbital plane at a distance of $R = 3a_b$	33

4.2	Trajectories of the simulations in $i\cos\Omega - i\sin\Omega$ phase space. Each trajectory starts at the black ‘×’ and spirals inwards counterclockwise towards the point (0.0, 0.5), with the final state of each simulation at 1000 binary orbits marked by the colored dots. Angular quantities are measured in reference to the binary orbital plane at a distance of $R = 3a_b$, as in Figure 4.1. Gray paths show the trajectories of test particle orbits, spaced by 10°	35
4.3	<i>Top:</i> Spherically integrated radial surface density profiles at $t = 1000$ binary orbits, plotted on a logarithmic scale. <i>Bottom:</i> Radially averaged disk eccentricity at $t = 1000$ binary orbits, calculated with Equation 16 of Shi et al. (2012).	37
4.4	Face-on midplane density profiles of the disk at $t = 675T_b$	39
4.5	Closeup of the vortex in the $\alpha = 10^{-5}$ simulation at $t = 692$ binary orbits. <i>Top left:</i> Gas midplane density. The local overdensity and spiral arm pairs are clearly visible. <i>Top right:</i> Local vorticity. Strong anticyclonic regions are indicated in blue. Spiral arms are visible as red diagonal lines in the vicinity of the vortex. In both plots, black curves show contours of density. <i>Middle:</i> Azimuthal density across the vortex center. <i>Bottom:</i> Radial density across the vortex center.	40
4.6	Snapshots of the $\alpha = 10^{-5}$ simulation, showing the local disk vorticity. In the left four panels, blue regions denote areas of large anticyclonic vorticity. The black contours highlight high-density regions ($\rho = 0.6\rho_{\max}$) within the disk midplane. <i>Far Left:</i> Early on, the RWI is triggered with an $m = 2$ mode, creating two vortices on opposite sides of the disk. <i>Left:</i> Differences in orbital velocities cause the vortices to move together and merge. <i>Middle:</i> The result is a single vortex which orbits at the inner edge of the disk. <i>Right:</i> The remaining vortex is long-lived, and persists until the end of the simulation. <i>Far Right:</i> Midplane disk density, showing the vortex as well as the multiple spiral arms. The density scale is shifted compared to Figure 4.5 in order to highlight the spiral arms.	42
4.7	Orbital motion of the vortex in the $\alpha = 10^{-5}$ simulation. <i>Top:</i> Orbital radius of the vortex. <i>Middle:</i> Orbital frequency, in units of the binary orbital frequency Ω_b . The dotted line shows the Keplerian orbital speed at the vortex’s orbital radius. <i>Bottom:</i> Vortex aspect ratio $\chi = r\Delta\phi/\Delta r$	43
5.1	Density contours of the polar-aligning disks at $t = 1000$ binary orbits. Horizontal slice shows disk density, along the plane of the binary. Disks in the $\alpha = 0.01, 0.001$, and 10^{-5} cases are broken; the inner disk in the $\alpha = 0.01$ simulation has momentarily reconnected with the outer disk as it precesses about the binary eccentricity vector.	45
5.2	Evolution of the warp profile for the viscous ($\alpha = 0.1$, left) and inviscid cases ($\alpha = 10^{-5}$, right). Each curve represents the z -component of the unit angular momentum vector \mathbf{l}_z as a function of radius. Curves are plotted every 100 binary orbits.	46

5.3	Motion of the warp for the viscous ($\alpha = 0.1$, left) and inviscid cases ($\alpha = 10^{-5}$, right). <i>Top row:</i> The ψ parameter plotted against the disk radius. Curves are plotted every 100 binary orbits as in Figure 5.2. <i>Middle row:</i> The radial location of the warp, determined as the local location of maximum ψ . For wave-like propagation, both the initial break and secondary wave propagation are plotted. <i>Bottom row:</i> The outward propagation velocity of the warp. The dotted line represents the local sound speed velocity of c_s at the warp radius.	47
5.4	Drift of the breaking radius observed in our polar-aligning disks in the bending wave regime. Each panel shows the normalized surface density of the disk every 100 binary orbits, for different disk viscosities. Colors are the same as in Figures 5.2 and 5.3. Vertical dashed lines indicate the location of the breaking radius for each snapshot.	49
5.5	Comparison of the simulated breaking radius to analytical predictions. <i>Top:</i> Analytical timescales as predicted from Equations (2.11) and (2.12). Here, r_{in} is calculated to be $2.2a_b$ (see text for details). <i>Bottom:</i> Surface density of the $\alpha = 10^{-5}$ simulation at $t = 100$ binary orbits, in units of the initial surface density profile Σ_0 . The breaking radius is denoted by the sharp dip in Σ/Σ_0 . In both plots, vertical dashed lines indicate the predicted locations of the breaking radius.	50
5.6	Inner regions of the $\alpha = 10^{-5}$ polar-aligning simulation, projected back onto a single plane. <i>Left:</i> Midplane density. The inner disk features an RWI vortex. <i>Center:</i> Disk eccentricity. The inner disk is somewhat eccentric. <i>Right:</i> Disk vorticity. Note the strong vorticity minimum at the location of the vortex.	51
5.7	Surface density and warp profile of the GW Ori simulation at $t = 0, 2500$, and $5000T_b$	52
5.8	Rendering of the multiple break simulation at $t = 1200$ binary orbits. The directions of \mathbf{L}_b and \mathbf{e}_b are indicated in the top right, with \mathbf{L}_b pointing into the page. The first two breaks at $7a_b$ and $28a_b$ are visible. There is a large warp at $35a_b$ that appears similar to a break, but the disk is not broken at this distance. See text for details.	54
5.9	Similar to Figure 5.5, but for the multiple break simulation. In this figure, each panel shows different choices of the inner radius, $r_{\text{in}} = 2.5a_b$ (top) and $r_{\text{in}} = 4.0a_b$ (middle). Both choices produce outer breaking locations that are roughly consistent with the observed breaks in the simulation. The bottom panel is from a simulation at a time of $1500T_b$	55
5.10	Azimuthal rotation angle plotted as a function of radial location and time. Areas in the same connected disk precess together, and create a band of the same color. By the end of the simulation, three distinct bands are visible, corresponding to the three disks in the simulation. The disk surface density profile at $t = 1500T_b$ (same as Figure 5.9) is also shown at right to compare the locations of the observed gaps.	57

6.1	Shell-averaged radial mass flux of the $\alpha = 10^{-5}$ simulation. The dashed line marks the approximate orbital distance of the vortex. Short-period outflows are visible close to the binary ($2a_b$) as thin red stripes. Long-period variability, associated with the orbital period of the vortex, is visible from $3 - 4a_b$ as alternating red and blue bands.	61
6.2	$\tau = t_{\text{align}}/t_p$ as calculated by Equation (2.14) for different values of α . The vertical line indicates the rough location of the break as seen in our low viscosity simulations.	63
6.3	Comparison of disk timescales using the analytic equations Eq. (2.11) and (2.12) to the precession time calculated by directly integrating Eq. (2.9) with the observed surface density. Dashed red and blue lines indicate the analytic solutions for t_c and t_p , while the solid blue line shows the directly integrated value for t_p	66
6.4	Analytic precession rates calculated from Eq. (2.32) of Farago & Laskar (2010) as a function of disk inclination, for the cases of the polar-aligning disks in Sec.5.1 (top) and the GW Ori system in Sec.5.2 (bottom). The vertical line denotes the critical inclination i_{crit} for this system; inclinations lower than i_{crit} align to a coplanar orientation, while inclinations higher than i_{crit} align to a polar orientation. Precession rates are normalized to T_0 , the precession rate for a nearly coplanar or nearly polar disk.	69
A.1	Example of the coordinate transform using a 2D slice of the simulation data at $t = 0$. <i>Top Row:</i> Coordinate grid lines for the simulation and disk coordinates. <i>Middle Row:</i> Disk density in the simulation and disk coordinates. <i>Bottom Row:</i> Azimuthal velocity v_ϕ in the simulation and disk coordinates.	80

CHAPTER 1

INTRODUCTION: MISALIGNED DISKS IN THE UNIVERSE

Protoplanetary disks are part of the early era of the star formation process. Despite consisting of the first 1-10 percent of the star's lifespan, this is an important stage of stellar evolution and events here can have large impacts on later stages of the stellar system. It is within these disks that the process of planet formation takes place, where the disk material coalesces into larger and larger bodies to form protoplanets. These protoplanets are the progenitors of exoplanetary solar systems, thousands of which have been discovered to date.

Our understanding of protoplanetary disks has improved drastically in the past decade thanks to observations from modern radio telescopes such as the Atacama Large Millimeter Array (ALMA), which have provided new insight into the disks' detailed structure (ALMA Partnership et al. 2015). The improved resolution provided by ALMA has revealed that many disks are not uniform, but instead have multiple substructures including rings, gaps, and crescents (Andrews et al. 2018). The presence of these substructures may suggest the existence of fluid instabilities or active planet formation within the disk (Bae et al. 2023), and there is a large amount of active research focused on explaining these observational features.

Stars are frequently formed in pairs or clusters during the collapse of a molecular cloud. Nearly 50% of Sun-like stars are born as part of a binary system, with the binary fraction increasing for higher mass stars (Duquennoy & Mayor 1991; Kouwenhoven et al. 2007; Offner et al. 2023). Thus, protoplanetary disks in multiple star systems, in the form of both circumbinary and smaller circumprimary disks, are expected to be a common occurrence (Monin et al. 2007). Analogous to how a protoplanetary disk around a single star can give

rise to planets, the circumstellar and circumbinary disks in a young binary star system may act as the birthsites of the S-type and P-type circumbinary planet populations, respectively (Dvorak 1986). Observations of binary star systems at different evolutionary stages have revealed different types of protoplanetary disks and planetary systems around binary stars, including circumbinary disks (Simon & Guilloteau 1992; Czekala et al. 2017; Kennedy et al. 2019; Bi et al. 2020; Kraus et al. 2020), individual circumstellar disks (Cruz-Sáenz de Miera et al. 2019; Keppler et al. 2020), and exoplanet systems in both S- and P-type orbits (e.g. Doyle et al. 2011; Martin 2018).

The orbits of the central stars in binary and higher-order star systems cause the gravitational field to vary over time, generating rich orbital dynamics which are unseen in single-star systems. This leads to many new phenomena unique to binary star systems. Close to the orbit of the central stars, there exists a region of dynamical instability, limiting the range of stable orbits for both S- and P-type planets (Dvorak 1986; Holman & Wiegert 1999; Quarles et al. 2018; Chen et al. 2020). Companion stars on wide orbits can perturb the system on long timescales, causing orbiting particles to undergo von Zeipel-Lidov-Kozai oscillations (von Zeipel 1910; Lidov 1962; Kozai 1962).

Polar-Aligning Disks

In the presence of a central binary, one might expect a circumbinary disk that is misaligned with the orbital plane of the binary to slowly align with the binary plane, such that the entire system's angular momentum lies along a single axis. Indeed, this is the case if the binary is circular. However, if the central binary is eccentric, then there exist stable

configurations in which the disk can be aligned perpendicular or nearly perpendicular to the binary plane.

The existence of such “polar disks” was first noticed through analytical considerations of orbits around binary systems in Farago & Laskar (2010). Numerical simulations (Aly et al. 2015; Martin & Lubow 2017, 2018) later confirmed this behavior in the context of circumbinary disks around black holes and young stellar objects. The first ALMA observations of polar disks appeared shortly afterwards. The most well-studied of these is the HD 98800 system (Kennedy et al. 2019), a hierarchical double binary system with a face-on circumbinary disk observed around the B binary component. The A and B binary systems orbit each other on a 67 AU orbit with a moderate eccentricity ($e \sim 0.5$), while the disk-hosting BaBb binary components lie on a highly eccentric orbit ($e \sim 0.8$) with separation 1 AU (Zúñiga-Fernández et al. 2021). Other disks have characteristics that suggest polar alignment, such as IRS 43 (Brinch et al. 2016). The binary components within this edge-on circumbinary disk are visible outside the circumbinary disk plane, implying a largely misaligned orbit. Both components of the binary are also surrounded by circumstellar disks, each angled differently to the external circumbinary disk, suggesting a complex accretion flow from the surrounding disk onto the central stars.

To date, all simulations of polar-aligning disks have been conducted using smoothed particle hydrodynamics (SPH) (e.g. Martin & Lubow 2017, 2018, 2019; Kennedy et al. 2019; Smallwood et al. 2019; Cuello & Giuppone 2019; Martin et al. 2022). These simulations make use of a high number of particles ($N \gtrsim 10^6$) in order to properly resolve the disk and capture its global dynamical evolution. However, the range of fluid viscosities that can be simulated with SPH is limited by the number of particles in a given region. The minimum effective

Shakura-Sunyaev α -viscosity (Shakura & Sunyaev 1973) that can be simulated with SPH is roughly $\alpha = 0.01$ for most simulations (Price et al. 2018). Protoplanetary disks around single stars have been found with viscosities of $\alpha \lesssim 10^{-4}$ (Pinte et al. 2016; Villenave et al. 2022), suggesting that the study of polar-aligning disks at low viscosities is an important but unexplored part of the overall parameter space.

Warped Disks

Many astrophysical disks have been observed to not lie entirely within a single orbital plane. These disks are generally referred to as “warped” disks, describing their non-planar geometry and changing orientation in three-dimensional space. Warped disks have been observed in many areas of astrophysics at all different scales, from planetary rings to the disks of galaxies (Burke 1957; Kerr et al. 1957; Shu et al. 1983; Burrows et al. 1995). Many other warped structures have been inferred from its effects on their nearby surroundings, including maser emission in the vicinity of supermassive black holes (Miyoshi et al. 1995; Martin 2008), as an explanation for long-term periodicity in close X-ray binaries (Katz 1973; Petterson et al. 1991; Scott et al. 2000), and as a source of shadows cast in protoplanetary disks (Marino et al. 2015; Debes et al. 2017).

The ubiquity of warped disks warrants careful study of its behavior and evolution. A large amount of work has gone into analytically deriving the evolution of a warp and testing this behavior via numerical methods (see Papaloizou & Pringle (1983); Pringle (1992); Papaloizou & Lin (1995); Ogilvie (1999); Lodato & Pringle (2007); Lodato & Price (2010), as well as Nixon & King (2016) for an overall review). In a warped disk, the angular momentum of

the disk \mathbf{L} changes with the disk radius r . The overall evolution of a warped disk can be broadly classified into two different behaviors, depending on the relative sizes of the disk aspect ratio h/r to its Shakura-Sunyaev α -viscosity coefficient (Shakura & Sunyaev 1973). Thin, high-viscosity disks with $\alpha > h/r$ are said to be in the *diffusive* or *viscous* regime, where the warp flattens diffusively on timescales inversely proportional to a second viscosity coefficient ν_2 . Thicker, low-viscosity disks with $\alpha < h/r$ are instead considered to be in the *bending wave* or *wave-like* regime, in which the pressure forces from the warp launch a wave which propagates through the disk.

In the diffusive regime, the evolution of a warped disk may be described as a diffusion equation in \mathbf{L} with terms proportional to the standard viscosity ν_1 and a warp viscosity ν_2 . Terms including ν_1 describe the standard viscous evolution of a flat disk (i.e. Lynden-Bell & Pringle (1974)), whereas terms including ν_2 describe the evolution of the warp in the disk (Pringle 1992). There are also additional terms present which include a third viscosity term ν_3 , causing precession of the disk as neighboring annuli induce a torque perpendicular to the direction of the warp (Ogilvie 1999). Subsequent works have also derived evolution equations in the bending wave regime in which the effects of pressure dominate over viscosity (Papaloizou & Lin 1995; Demianski & Ivanov 1997; Lubow & Ogilvie 2000), as well as more general sets of equations that encompass both regimes (Martin et al. 2019; Dullemond et al. 2022).

The relative sizes of the viscosity coefficients ν_1 , ν_2 , and ν_3 also depend on the amplitude of the warp, characterized by the dimensionless parameter ψ defined as

$$\psi = r \left| \frac{\partial \mathbf{l}(r)}{\partial r} \right|. \quad (1.1)$$

where \mathbf{l} is the local angular momentum vector of the annulus at radius r . The dependence of the coefficients on ψ for large, non-linear warps and the disk viscosity α is characterized in Ogilvie (1999).

When warps become very large, the disk may be unable to communicate across the warp effectively. The warp may become unstable, and disk breaking can occur, splitting the disk into separate rings. This phenomenon has been studied analytically (Doğan et al. 2018; Raj et al. 2021), and previously observed in simulations of circumbinary systems, as well as disks around single and binary black holes (Larwood et al. 1996; Nixon et al. 2012, 2013; Nealon et al. 2015). Disk breaking is also thought to have occurred in some systems as a possible explanation for the observed geometry or accretion kinematics (Casassus et al. 2015; Facchini et al. 2018; Zhu 2019; Kraus et al. 2020; Nealon et al. 2022). However, the exact conditions that lead a disk to break are still unclear, as well as where the location of the break (known as the breaking radius) will occur.

Warped disks, similar to polar-aligning disks, have primarily been studied using SPH codes. Since resolution in Lagrangian codes is determined by the local particle density, the area in the vicinity of a disk breaking event is of some concern. The process of the initial breaking event, as well as the subsequent evolution of the break and interaction between the misaligned inner and outer disks involve sparse regions, and may be poorly characterized in SPH simulations unless large numbers of particles are used.

In this work, we plan to expand on the previous results for polar-aligning and warped

protoplanetary disks by using a grid-based hydrodynamic code to simulate inclined circumbinary disks. The resolution of grid-based codes is limited by the fineness of the grid instead of the particle density, which allows them to reach lower viscosities and resolve both high and low density regions equally. We will use the increased range of α -viscosities to explore polar disks in the low-viscosity regime, as well as simulate warped and broken disks in both the diffusive and bending wave regimes. Additionally, we take advantage of the fact that disk breaking occurs more easily for disks that are aligning towards a polar orientation, compared to a coplanar orientation, around binaries on an eccentric orbit.

This work is organized as follows. In Chapter 2 we outline the timescales of disk evolution relevant to disk breaking and describe a new analytic method of calculating the location of a break. In Chapter 3 we outline the numerical methods used to simulate an inclined circumbinary disk, as well as the various simulation setups used to examine both polar-aligned and warped disks. Chapter 4 displays the results of the simulations pertaining to polar-aligning disks, and Chapter 5 contains the results for the simulations of warped and broken disks. In Chapter 6, we discuss the implications of our results to planet formation in circumbinary disks and potential observational signatures with current telescopes. Finally, we present our conclusions in Chapter 7.

CHAPTER 2

TIMESCALES OF DISK EVOLUTION

Contributing Authors: Zhaohuan Zhu (University of Nevada, Las Vegas), Rebecca Martin (University of Nevada, Las Vegas), Stephen Lubow (Space Telescope Science Institute)

In this chapter, we examine the different evolutionary timescales that affect a warped disk, and consider how these timescales determine the breaking radius of the disk. In doing so, we derive an analytic criteria for determining the disk breaking radius. We consider the situation of a circumbinary disk surrounding a central binary. The binary consists of two stars with masses M_1 and M_2 , with total mass labeled $M_{\text{tot}} = M_1 + M_2$, orbital semi-major axis a_b , and orbital eccentricity e_b . We choose radial power-law profiles for midplane density, temperature, and surface density, using the indices d , s , and p given by ¹

$$\rho(r) = \rho_0 \left(\frac{r}{r_0} \right)^{-d}, \quad (2.1)$$

$$T(r) = T_0 \left(\frac{r}{r_0} \right)^{-s} \quad (2.2)$$

and

$$\Sigma(r) = \Sigma_0 \left(\frac{r}{r_0} \right)^{-p}. \quad (2.3)$$

¹Previous works commonly use p for the midplane density index but are inconsistent in using q for either the temperature or sound speed index. There is also some inconsistency when considering the sign of the index, i.e. if the negative sign of the exponent is included in the variable (e.g. Takeuchi & Lin (2002)). We choose positive indices and our variable names to remain consistent with the variables in Lubow & Martin (2018), and to avoid confusion with the variable used for the binary mass ratio.

For a steady state Keplerian disk, these power-law indices are related through the equation

$$2d + s - 2p = 3 \quad (2.4)$$

since $\rho = \Sigma/H$ (e.g. Pringle 1981) and the sound speed of the disk is given by $c_s = h\Omega \propto T^{1/2}$.

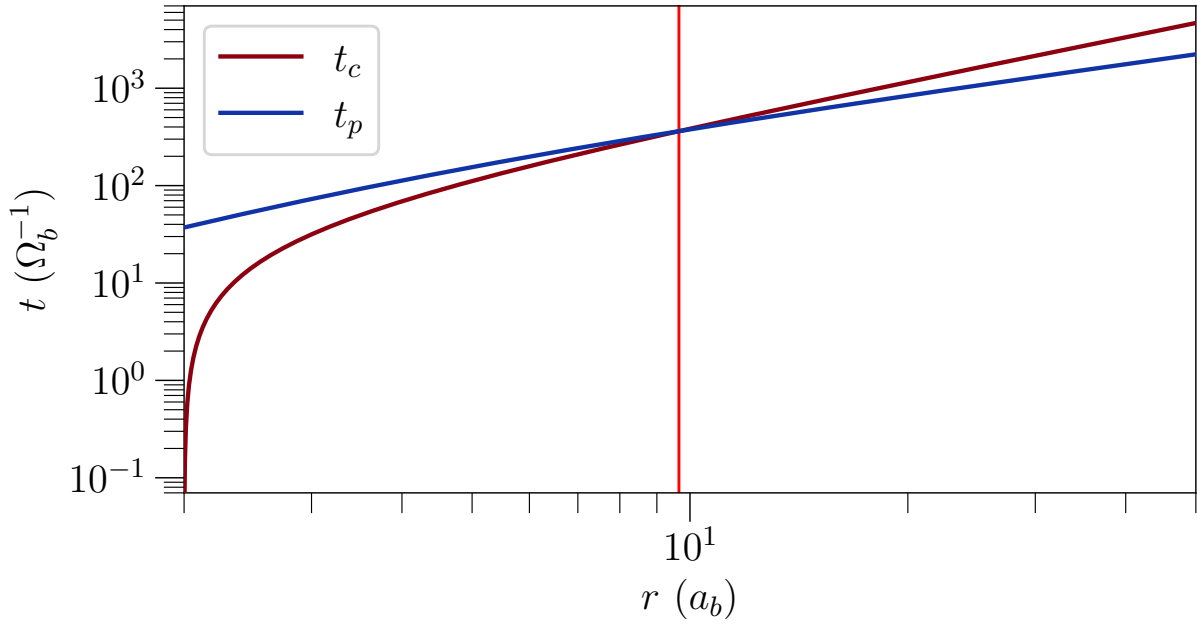


Figure 2.1: Disk timescales t_p and t_c as a function of disk radius on a logarithmic scale. The red vertical line indicates the expected location of a disk breaking event based on Equations (2.11) and (2.12). For this figure, we consider a nearly coplanar disk around an equal mass binary with $e_b = 0.5$, extending from $r_{\text{in}} = 2a_b$ to $r_{\text{out}} = 50a_b$. The disk has a constant scale height $h/r = 0.1$, with power law slopes of $p = 1.5$ and $s = 1.0$.

2.1 Disk Breaking in the Wave-like Regime

The central binary exerts a torque on the disk, causing it to precess. For a ring of material with radius r , the torque excites a nodal precession with frequency:

$$\omega_p(r) = k \left(\frac{a_b}{r} \right)^{7/2} \Omega_b \quad (2.5)$$

(e.g. Farago & Laskar 2010), where Ω_b is the orbital frequency of the binary, r is the radius of the ring, and k is a constant which depends on the binary masses, eccentricity, and whether the disk is close to a coplanar or polar configuration (Aly et al. 2015; Martin & Lubow 2017; Zanazzi & Lai 2018; Lubow & Martin 2018; Martin & Lubow 2018). For a circumbinary disk, the inner regions feel a stronger torque from the binary than the outer regions. In the absence of communication between adjacent annuli, the inner rings precess faster than the outer rings. Therefore, depending upon the communication timescale between the rings that make up the disk, the disk may become warped.

If the radial communication timescale is short compared with the precession timescale then the disk can precess like a solid body. For a disk with inner radius r_{in} and outer radius r_{out} , the global precession timescale t_p of the disk as a solid body is given by

$$t_p = \frac{2(1+p)r_{\text{in}}^{1+p}r_{\text{out}}^{5/2-p}}{|k|(5-2p)a_b^{7/2}\Omega_b}. \quad (2.6)$$

and the radial communication timescale in the wave-like regime t_c is given by

$$t_c = \frac{4}{(2+s)\Omega_b h_{\text{out}}} \left(\frac{r_{\text{out}}}{a_b} \right)^{3/2} \quad (2.7)$$

(Eqs. (33) and (31) of (Lubow & Martin 2018)) where h_{out} is the scale height at the outer edge of the disk.

We expect disk breaking to occur when the global precession timescale is shorter than the communication timescale, $t_p < t_c$. Analytic estimates of the disk breaking radius have been given in many previous works (e.g. Nixon et al. 2013; Lubow & Martin 2018). Combining Equations (2.6) and (2.7) and solving for r_{out} as the breaking radius gives

$$r_{\text{break}} = \left[\frac{(p+1)(s+2)h_{\text{out}}}{2(5-2p)|k|} \left(\frac{r_{\text{in}}}{a_b} \right)^{p+1} \right]^{\frac{1}{p-1}} a_b. \quad (2.8)$$

The timescales given in Equations (2.6) and (2.7) assume that $r_{\text{in}} \ll r_{\text{out}}$, i.e. that the disks have a large radial extent. During breaking events, a newly separated ring may be radially thin, so a more complete description of these equations is required.

Here we attempt to derive a more refined estimate of t_p and t_c by revisiting these equations. The disk nodal precession frequency is given in Equations (16)-(17) of Lubow & Martin (2018) as

$$\omega_p = k \frac{\int_{r_{\text{in}}}^{r_{\text{out}}} \Sigma r^3 \Omega (a_b/r)^{7/2} dr}{\int_{r_{\text{in}}}^{r_{\text{out}}} \Sigma r^3 \Omega dr} \Omega_b \quad (2.9)$$

where Ω is the orbital frequency and k is a general constant depending on the parameters of the binary. Equation (16) of Lubow & Martin (2018) and Equation (5) of Smallwood et al. (2019) give the value of k as

$$k = \begin{cases} -\frac{3}{4} \sqrt{1 + 3e_b^2 - 4e_b^4 \frac{M_1 M_2}{M_{\text{tot}}^2}} & \text{for a nearly coplanar disk,} \\ \frac{3}{4} \sqrt{5} e_b \sqrt{1 + 4e_b^2 \frac{M_1 M_2}{M_{\text{tot}}^2}} & \text{for a nearly polar disk.} \end{cases} \quad (2.10)$$

The fraction containing the binary masses $M_1 M_2 / M_{\text{tot}}^2$ may also be written as $q / (1 + q)^2$, where $q = M_2 / M_1$ is the binary mass ratio. Equation (2.10) implies that the value of k is largest (and thus the precession rate quickest) for equal mass binaries. Low eccentricity binaries produce larger k values for coplanar disks, while higher eccentricity binaries give larger values of k for polar disks. When applied to disk breaking, larger values of k reduce the precession timescale, and thus are more favorable for producing a break. The sign of k also determines the direction of precession; a positive value of k denotes counterclockwise precession around the precession vector, while a negative value of k signifies clockwise precession.

We define the disk precession time to be $t_p = 1 / \omega_p$. Evaluating the integrals in Equation (2.9) for a disk with the surface density profile in Equation (2.3) and Keplerian rotation profile $\Omega = \Omega_K \propto r^{-3/2}$, we find for the disk precession time

$$t_p = \frac{-2(1+p)}{k(5-2p)\Omega_b} \left(\frac{r_{\text{in}}}{a_b}\right)^{7/2} \left[\frac{(r_{\text{out}}/r_{\text{in}})^{5/2-p} - 1}{(r_{\text{out}}/r_{\text{in}})^{-(1+p)} - 1} \right]. \quad (2.11)$$

In the limit that $r_{\text{out}} \gg r_{\text{in}}$, the expression above simplifies to Equation (2.6).

To calculate the communication time of a warp across the disk, we consider the travel speed of bending waves starting from the inner edge. These waves travel at half the local sound speed (Papaloizou & Lin 1995). Assuming a radial power-law profile for the disk temperature as in Equation (2.2), we calculate the radial communication time as

$$t_c = \int_{r_{\text{in}}}^{r_{\text{out}}} \frac{2}{c_s(r)} dr = \frac{4}{s+2} \left[r_{\text{out}}^{s/2+1} - r_{\text{in}}^{s/2+1} \right]. \quad (2.12)$$

An example of these timescales are shown as a function of disk radius in Figure 2.1. For geometrically thin rings, $r_{\text{in}} \approx r_{\text{out}}$, Equations (2.11) and (2.12) reproduce the correct limiting behavior ($t_p \approx 1/\omega_p$ and $t_c \approx 0$), which Equations (2.6) and (2.7) do not.

Using Equations (2.11) and (2.12), we can derive an updated location for the breaking radius. In regions of the disk where $t_p > t_c$, a precession induced warp can be communicated via bending waves and allow the disk to precess rigidly. We take the breaking radius r_{break} to be the smallest value of r_{out} for which $t_p = t_c$; for $r_{\text{out}} > r_{\text{break}}$ we have that $t_p < t_c$ and the disk will precess faster than it is able to communicate the precession to its outer edge, causing the disk to break. This criterion approximately says that the breaking radius occurs at the distance that a bending wave can travel over a disk precession timescale, starting from the disk inner edge.

Whether the curves of t_p and t_c intersect is determined by the disk *geometry* ($r_{\text{in}}, r_{\text{out}}, h/r$), disk *structure* (power-law slopes d , s , and p), and inner binary arrangement (q , a_b , and e_b , which determine the constant k). The slope of Equation (2.11) is determined by the surface density power-law slope p and the ratio $r_{\text{out}}/r_{\text{in}}$, whereas the slope of Equation (2.12) is determined by the temperature power-law slope s . The location of the inner radius, r_{in} , sets the fastest precession rate of the entire disk and the initial height of the t_p curve, and is a strong factor in determining whether or not a disk will break. Because of this sensitive dependence on r_{in} , nearly polar aligned disks are more likely to have breaks (Section 3.2 and 3.3), as the large misalignment reduces the strength of the binary torque, which allows the disk to maintain smaller inner cavities (Miranda & Lai 2015; Franchini et al. 2019) and therefore faster precession rates. In addition, for fixed binary and disk parameters, the precession rate (normalized by binary frequency) of a nearly polar disk is faster than that of a

nearly coplanar disk for binary eccentricities $e_b > 0.41$, as follows from Equation (2.10).

Once the disk breaks into separate rings, the outer disk will have a new inner radius at the location of the break and its timescales will be reset. These timescales can grow again starting from the inner edge of the outer disk and, depending on the conditions of the outer disk, they may intersect again and cause the outer disk to break into yet another set of rings. Thus, if our analytic equations are applied repeatedly, our breaking condition could predict the breaking radii of multiple breaks. In Section 2.4, we explore the possibility of multiple disk breaking in more detail, examining which disk parameters are required to cause multiple disk breaking.

2.2 A Criterion for Viscous Disk Breaking

Disks align towards their precession vector (L_b for coplanar orientations, or e_b for polar orientations) in both the wave-like and viscous regimes on a timescale that is roughly inversely proportional to α (King et al. (2013), Lubow & Martin 2018, Eq.29)

$$t_{\text{align}} = \frac{(h/r)^2 \Omega_b}{\alpha (\omega_p)^2}. \quad (2.13)$$

If the alignment timescale is significantly faster than the precession rate, the disk will align to the precession vector before it can precess a significant amount. This can suppress large warps generated by azimuthal “twisting” motions (Raj et al. 2021), which may prevent disk breaking even if the other disk parameters would normally allow a break to occur. We can express this relation by finding the ratio of t_p to t_{align}

$$\tau(r) = \frac{t_{\text{align}}}{t_{\text{p}}} = \frac{(h/r)^2}{\alpha} t_{\text{p}} \Omega_{\text{b}}. \quad (2.14)$$

When this ratio is less than 1, $t_{\text{align}} < t_{\text{p}}$ and alignment occurs before disk precession, preventing disk breaking. This criterion is primarily applicable to disks in the diffusive regime, although the factor of $(h/r)^2/\alpha$ suggests it may apply to some disks in the wave-like regime as well. Equation (2.14) is a simple estimate which only considers the disk scale height at one particular radius; other approaches may take into account how the scale height changes radially across the disk.

Various disk breaking criteria have been suggested in the past. Equation (13) of King et al. (2013) considers $t_{\nu_2} \omega_{\text{p}} < 1$ as the criterion to prevent large disk warping in the viscous regime, where t_{ν_2} is the viscous timescale associated with the ν_2 viscosity. We note that in the linear regime of small warps, this criterion and the Equation (2.14) give opposite stability results because $(\omega_{\text{p}} t_{\text{align}})^{-1} \sim \omega_{\text{p}} t_{\nu_2}$. A short (long) alignment timescale occurs with a long (short) warp viscous timescale. However, the ν_2 value used for small warps may not apply for cases of disk breaking.

2.3 An Application to GW Orionis

GW Orionis is a hierarchical triple star system surrounded by a large protoplanetary disk (Mathieu et al. 1991; Berger et al. 2011). Resolved images of the system (Bi et al. 2020; Kraus et al. 2020) show a series of dust rings in differing orientations around the central star system as well as distorted velocity maps in ^{12}CO , suggesting that the disk is warped. Observations indicate that the outer disk is inclined with respect to the outer binary orbital

plane at an angle of roughly $i = 38^\circ$.

The GW Orionis system has been simulated in previous works, but simulations have shown differing results as to whether the disk will break solely under the influence of the inner star system. In their observational paper, Kraus et al. (2020) use SPH simulations to explain the warped geometry of the system. They simulate the GW Ori disk with an initial radial range of 40 to 200 au, using power-law slopes of $p = 0.2$ and $s = 1.0$ and a very thin disk with $h/r = 0.02$. The disk expands inwards until the inner radius reaches about 30au, where a thin ring breaks off from the inner edge of the disk and precesses independently, eventually aligning with the binary plane. Kraus et al. (2020) interpret this inner ring as a potential origin of the R3 dust ring seen in observations.

Bi et al. (2020) and Smallwood et al. (2021) ran a similar suite of SPH simulations for the GW Ori system, using a disk with the same initial inner edge but a slightly thicker aspect ratio of $h/r = 0.05$ and power-law slopes of $p = 1.5$ and $s = 1.0$. Their simulations find a disk that warps strongly but does not break through disk precession alone. They suggest that a giant planet embedded in the disk is required to carve a gap first in order for an inner ring to break off. However, they find that a disk with a smaller inner radius, $r_{\text{in}} = 20\text{au}$, can spontaneously generate a break, with a breaking radius of roughly 75 au. From this, they determine that the geometry of the disk is an important factor in determining if a disk is able to break.

By applying Equations (2.11) and (2.12) to the GW Orionis system, it is possible to explain the appearances of both SPH simulations. To model this triple star system with our analytic equations, we assume that the triple star orbit can be approximated by the outer binary orbit of the triple. This assumption is justified for a low binary eccentricity (e.g.

Lepp et al. 2023; Smallwood et al. 2021). The components of the outer binary are composed of two masses with $M_1 = 0.742M_{\text{tot}}$ and $M_2 = 0.258M_{\text{tot}}$ and an eccentricity of $e_b = 0.379$. Including the effect of the inner binary will cause apsidal precession in the orbit of the outer binary (Lepp et al. 2023), but we do not consider this effect when considering the precession of the disk. We use the parameters from two disk models listed above, with the size of r_{in} varying from 40au to 20au to simulate the inward drift of the disk.

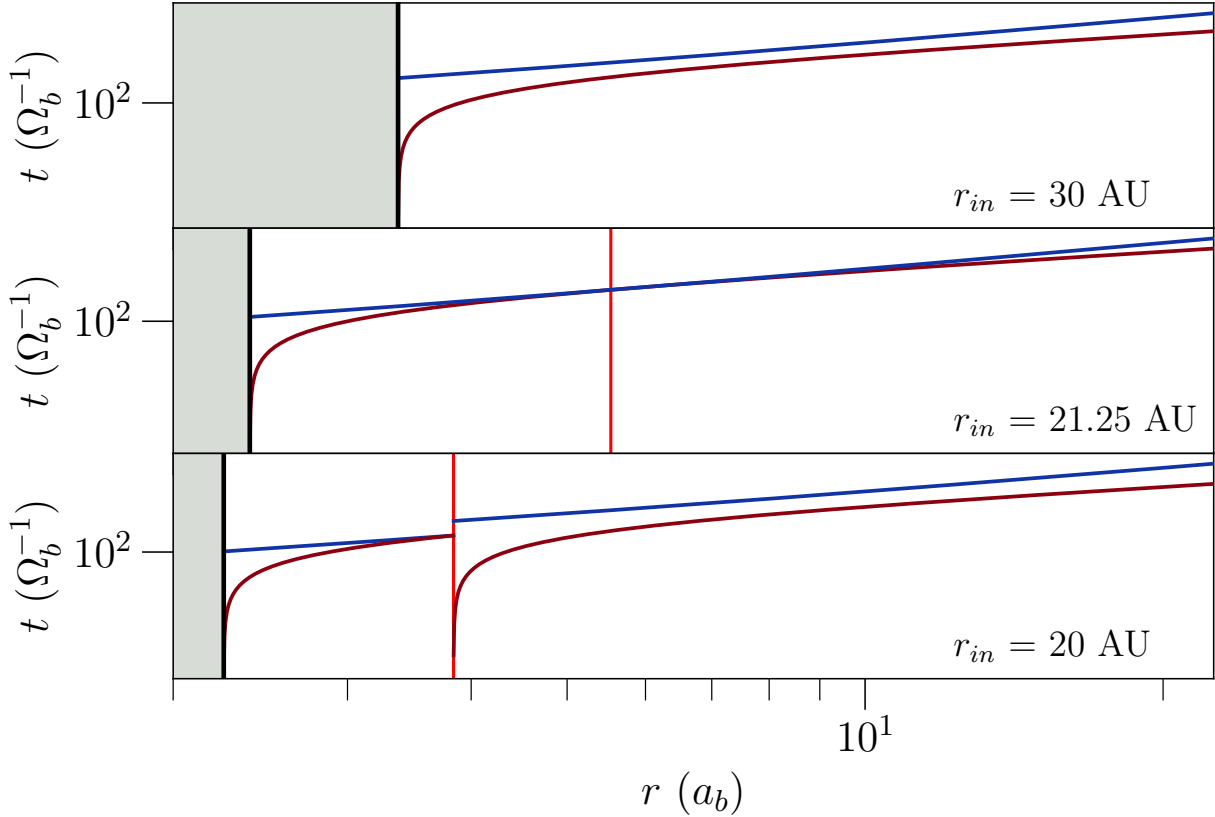


Figure 2.2: Predicted disk evolution of the Kraus et al. (2020) parameters, as inferred from our timescale equations. In each panel the lines are the same as Fig. 2.1. The shaded region indicates the inner cavity of the disk. *Top*: Early on, the inner edge of the disk is far enough out that a break does not occur. *Middle*: As the disk evolves, the inner edge drifts inwards until $r_{\text{in}} = 21.25$ au, where a break spontaneously occurs at 49 au. *Bottom*: As the inner edge continues to drift inwards, so does the expected breaking radius. Once the inner disk reaches an inner radius of 20 au, the expected breaking radius has moved to a radius of roughly 35 au.

For the Kraus et al. (2020) simulation, the initial conditions have $t_p > t_c$ everywhere, indicating a disk with no breaks. However, the two curves approach as the inner edge of the disk drifts inward. Once the inner edge of the disk reaches about 21au, the two curves intersect and a break spontaneously appears at $r_{\text{break}} = 49\text{au}$, producing a thin secondary ring along the inner edge. By the time the inner cavity has shrunk to 20au, the breaking radius has also moved inwards to a distance of $r_{\text{break}} = 35\text{au}$, a distance that is consistent with the observed location of the ring seen in the SPH simulations. Figure 2.2 illustrates the evolution of t_p and t_c in the Kraus disk model. If spontaneous disk breaking occurs in this manner, the material in the inner ring can be shuttled inward into a tight ring similar to what is seen in the GW Ori observations.

The disks used by Bi et al. (2020) and Smallwood et al. (2021) are thicker and have a higher disk temperature, creating smaller values for t_c . Although the two curves begin to intersect at nearly the same value of r_{in} , the change in the shape of the curves causes the value of r_{break} to start from the outer edge of the disk and sweep inwards, instead of starting in the middle like the Kraus et al. (2020) disk. The inner cavity must shrink even more, down to $r_{\text{in}} = 15\text{au}$, in order for the break to produce a similarly confined inner ring. This model is unlikely to break the disk using the binary torque alone, making a planet-driven explanation more likely for these disk parameters.

By comparing these simulations, it is clear that the details of the simulation parameters are important in determining the location of a disk break. Observations of the GW Ori system are currently unable to put strong constraints on the disk parameters, so the GW Ori disk may be able to break under the torque of the binary if it is closer to the Kraus et al. (2020) simulation, i.e. cooler and with lower values of h/r . In Section 3.3, we describe our

simulations for the GW Ori system.

2.4 Multiple Disk Breaking

After a disk breaks into two, the inner and outer disk will begin to precess independently. The inner disk is guaranteed to precess rigidly, by the conditions set by the break, but the outer disk may once again precess differentially with its own t_c and t_p starting from the initial breaking radius, which is its new inner edge. If this new outer disk has a breaking radius that is within the radial extent of the outer disk, then the outer disk may break again. This process of *multiple disk breaking* can repeat and break the disk into several rings for as long as there is disk material, or until the estimates for t_c and t_p above are no longer valid. Some SPH simulations have observed this phenomenon previously, in the context of disks around black hole binaries and the Bardeen-Petterson effect (Nixon et al. 2013; Nealon et al. 2015).

To get a better understanding of how the various disk parameters affect the number of disk breaks, in Figure 2.3 we map out the number of disk breaks for different initial values of r_{in} , r_{out} , and $(h/r)_0$ (the disk geometry) and as a function of the power-law slopes p and s (the disk structure). In this figure, the disk is placed around an equal mass binary ($M_1 = M_2 = 0.5$) with $e_b = 0.5$. Each panel shows the number of expected disk breaking events for the given initial disk geometry as a function of p and s . In each panel, the horizontal line at $s = 1$ represents disks with a constant h/r throughout; points below this line represent flaring disks, with h/r increasing with radius. In general, disks that are thin, have small inner cavities, and steep power-law profiles are more likely to have multiple

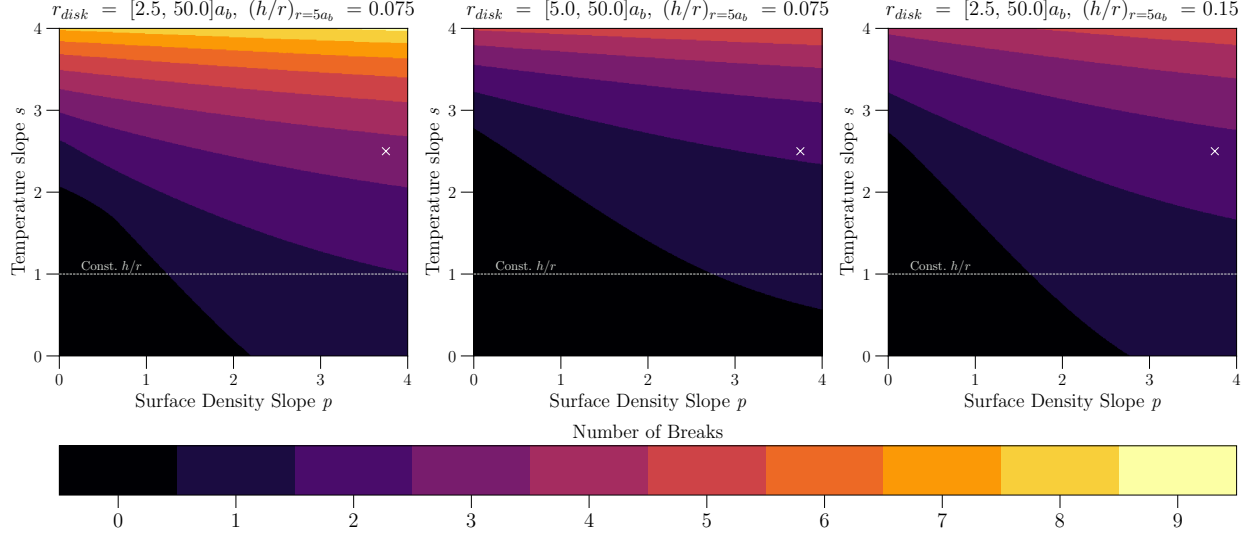


Figure 2.3: Predicted number of breaks for a disk with a given initial geometry, shown as a function of the surface density and temperature power-law exponents p and s . The radial extent of the disk is given as $r_{\text{disk}} = [r_{\text{in}}, r_{\text{out}}]$ and the initial scale height is given at a distance of $r = 5a_b$. The central binary is an equal mass binary with eccentricity $e_b = 0.5$. *Left*: Initial inner radius and scale height. *Middle*: Effect of a larger inner disk radius. *Right*: Effect of a larger disk aspect ratio. The ‘ \times ’ in each panel marks the disk parameters used in our multiple break simulation (Section 3.4).

breaks.

The effect of changing the inner radius can be seen by comparing the first and second panels. Doubling the inner radius reduces the number of breaks in each region by roughly 1 each. This behavior is consistent with the disk breaking seen in the simulations of Smallwood et al. (2021), who also noticed that disk breaking was dependent on the size of the inner cavity. Tidal interactions from the binary component can truncate the disk edges, providing limits on the values of r_{in} and r_{out} (Larwood et al. 1996; Lubow et al. 2015; Miranda & Lai 2015). Miranda & Lai (2015) study tidal truncation of circumbinary disks due to Lindblad torques and find that for highly inclined disks, the inner radius is truncated close to the 1:3 and 1:4 commensurabilities, approximately 2.0 to 2.5 a_b . Figure 2.3 also shows that

increasing the disk scale height increases the width of each "stripe", requiring a steeper temperature gradient to achieve multiple breaks. For typical protoplanetary disk parameters, disk breaking will usually be limited to a single break unless the disk is extremely thin. However, multiple breaking may still occur naturally when considering other sources of precession, such as around black holes.

CHAPTER 3

METHODS

Contributing Authors: Zhaohuan Zhu (University of Nevada, Las Vegas), Rebecca Martin (University of Nevada, Las Vegas), Stephen Lubow (Space Telescope Science Institute)

To study the behavior of misaligned circumbinary disks, we have developed a new simulation setup that is specialized towards the study of these systems. We use the simulation code ATHENA++ (Stone et al. 2020) to solve the incompressible Navier-Stokes equations. Our simulation considers an protoplanetary disk situated around a central binary star system and inclined to the binary orbital plane. An example of the simulation setup is shown in Figure 3.1.

All values in the simulation use spherical-polar coordinates (r, θ, ϕ) , with θ the polar angle and ϕ the azimuthal angle. The simulation domain extends from 5° to 175° in θ , and spans the full azimuthal range from 0 to 2π in ϕ . The radial extent of the domain can be adjusted for each problem to fit the specific disk being simulated. We divide the angular domain into 176 uniformly spaced cells in θ and 384 cells in ϕ .

We initialize the density and temperature profile of the disk using the radial power-law profiles listed in Equations 2.1 and 2.2:

$$\rho(r) = \rho_0 \left(\frac{r}{r_0} \right)^{-d} \quad (3.1)$$

$$T(r) = T_0 \left(\frac{r}{r_0} \right)^{-s} \quad (3.2)$$

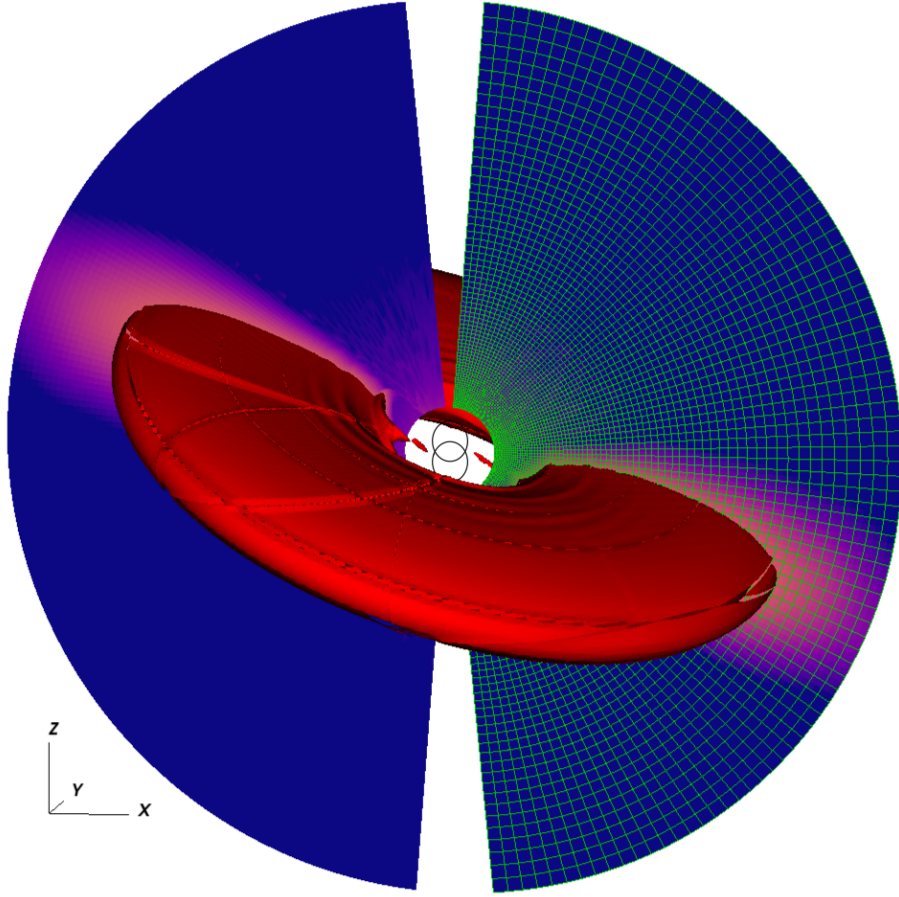


Figure 3.1: Example of the inclined disk simulation setup.

where ρ_0 and T_0 are the density and temperature at the reference radius r_0 . The vertical density profile is set by numerically integrating the density at each grid cell to establish hydrostatic equilibrium to match the disk scale height $h = c_s/\Omega_K$. We instate a spherically symmetric density floor across the domain which has the same power-law form as Equation 2.1, but with a leading constant of $\rho_{\text{floor}} = 10^{-4}\rho_0$.

The disk is initialized with a scale height of $(h/r)_0$ at r_0 , and follows a power-law profile determined by Equation 2.2. We implement the orbital cooling scheme outlined in Equation (5) of Zhu et al. (2015), using a dimensionless cooling time of $t_{\text{cool}} = 0.01\Omega_K^{-1}$. The binary components are simulated as gravitational bodies with masses M_1 and M_2 , which orbit with

semi-major axis a_b and eccentricity e_b . To set the radial limits of the disk, we truncate the edges of the disk using exponential cutoffs of the form $\exp[(r - \mu_r)/\sigma_r]$, with μ_r the location of the edge and σ_r the scale length of the cutoff. We misalign the disk with an initial inclination i by converting from simulation coordinates to tilted disk coordinates (Eq. (44) of Zhu 2019, also see the Appendix). Since the axis of rotation of the disk is now within the simulation domain, regions near the disk’s poles are initialized with a velocity

$$v = \sqrt{\frac{GM_{\text{tot}}}{r} \frac{r_{\text{cyl}}}{r}}, \quad (3.3)$$

where r_{cyl} is the cylindrical radius from the rotational axis. This prevents excessively high velocities near the rotational axis.

For the fluid simulation, we use the vl2 second-order van Leer predictor-corrector time integrator (Stone & Gardiner 2009) and either second or third-order PLM/PPM reconstruction. Close to the inner radial boundary, where $r < r_{\text{cyl}}$, we reduce the kinematic viscosity ν using an exponential cutoff such that

$$\nu = \alpha \frac{c_s^2}{\Omega_K} \exp\left(\frac{R - R_{\text{min}}}{0.268}\right). \quad (3.4)$$

This cutoff prevents the diffusive timestep from becoming too small and restricting the simulation speed, while only affecting a small region in the innermost areas of the simulation domain. This cutoff region resides within the inner cavity of the disk and is usually cleared of material by the binary torque in most simulations, so there are minimal effects on the overall results.

Lastly, the binary components are simulated as point masses orbiting within the inner

Parameter	Polar (§3.1)	Warped Polar (§3.2)	GW Ori (§3.3)	Multibreak (§3.4)
M_1	0.5	0.5	0.742	0.5
M_2	0.5	0.5	0.258	0.5
e_b	0.5	0.5	0.379	0.5
$\mu_{r,\text{in}}(a_b)$	2.0	2.0	2.7	2.0
$\sigma_{r,\text{in}}(a_b)$	0.35	0.35	0.35	0.35
$\mu_{r,\text{out}}(a_b)$	5.0	-	-	-
$\sigma_{r,\text{out}}(a_b)$	1.8	-	-	-
$(h/r)_0$	0.103	0.103	0.075	0.251
$i_0(^{\circ})$	60	60	38	60
d	2.25	2.25	2.5	4.0
s	1.5	1.5	1.0	2.5
p	1.5	1.5	1.5	3.75
α	$10^{-1},^{-2},^{-3},^{-5}, 0.05$	$10^{-1},^{-2},^{-3},^{-5}$	10^{-5}	10^{-5}

Table 3.1: Table of parameters used in the simulations. Parameters are sorted in groups of binary arrangement (top), disc geometry (middle), and disk structure (bottom).

radial boundary of the simulation, with masses M_1 and M_2 , orbital semi-major axis a_b , and orbital eccentricity e_b . We integrate the motion of the binary components using a 2nd-order leapfrog integrator, but we do not model the change in the orbits due to interaction with the disk material. We use a subcycling timestep method to ensure high accuracy of the binary orbit, independent of variations in the size of the CFL fluid timestep of the ATHENA++ fluid simulation.

We have conducted several sets of simulations which investigate the behavior of polar and warped disks. A summary of the simulation parameters is listed in Table 3.1. Below, we discuss each set of simulations in detail.

3.1 Polar-Aligning Disks

In our first set of simulations, we study the polar alignment of a disk using grid-based simulations. A disk that begins with an inclination angle in the range for polar alignment will

nodally precess about the binary eccentricity vector. Therefore, we rotate the system such that the binary orbits in the xz -plane of the simulation, with the binary angular momentum vector \vec{L}_b pointing along the positive y -axis and the eccentricity vector \vec{e}_b pointing along the positive z -axis. With this arrangement of the binary, a disk aligning towards the binary’s “polar” orientation will settle towards the xy -plane of the simulation domain ($\theta = \pi/2$). The use of this binary orientation keeps the disk from precessing outside of the spherical-polar domain during the simulation. This setup has the additional benefit of orienting the major axes of the central binary system towards the poles of the spherical-polar domain, which prevents strong gravitational interactions from occurring at the binary apoapsis and allows the inner radial boundary to be made as small as possible.

The geometric setup of the disk and binary system is shown in Figure 3.2, with the inclination angle i and ascending node Ω labeled. The angles i and Ω are measured relative to the binary plane using the equations

$$i = \arccos\left(\frac{L_y}{L}\right) \quad (3.5)$$

and

$$\Omega = \arctan\left(\frac{L_z}{L_x}\right), \quad (3.6)$$

where L_x , L_y and L_z are the components of the disk angular momentum L_{disk} in the simulation x , y and z axes.

Our binary and disk setup is based on the setup used in Martin & Lubow (2017). The central binary is chosen to be an equal-mass binary with eccentricity $e_b = 0.5$. This sets the

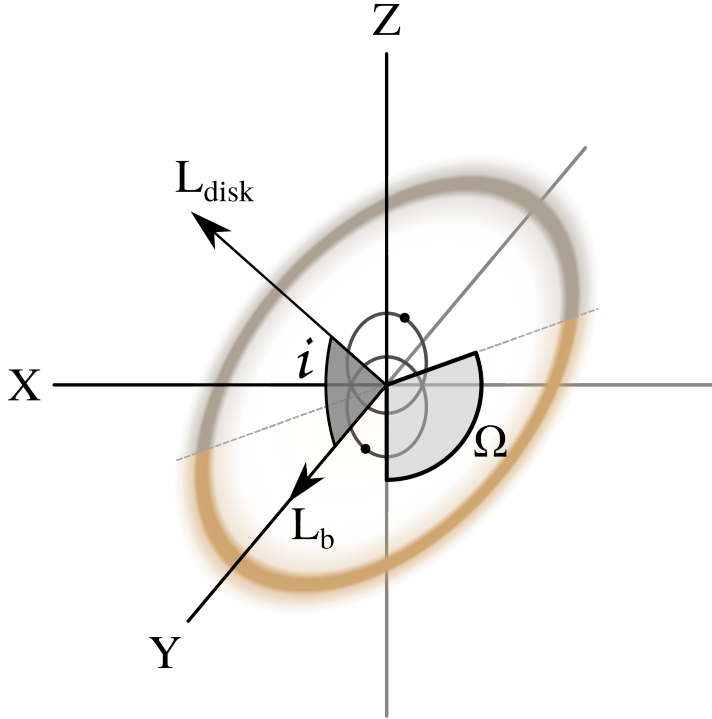


Figure 3.2: Schematic of the central binary and circumbinary disk arrangement used for polar disk simulations, as well as the angles used to measure the disk orientation. The binary orbits in the xz -plane, with the angular momentum vector L_b pointing along the positive y -axis and the eccentricity vector e_b pointing along the z -axis. The disk is oriented in 3D space by its angular momentum vector L_{disk} , where it forms an angle i with the vector L_b . The gray dashed line denotes the disk’s “line of nodes”, where the disk crosses the xz -plane at an angle Ω with the vector e_b as a reference direction.

initial tilt required for polar alignment of the disk at $i_{\text{crit}} = \arcsin \sqrt{3/8} \simeq 38^\circ$, based on the behavior of test particles Farago & Laskar (2010). For massive disks, the critical angle changes due to the exchange of angular momentum between the disk and the binary (Martin & Lubow 2019). Since for our simulations the binary does not feel the gravitational force from the disk and self-gravity is not included, the disk can be considered to be in the low mass regime. The disk is truncated at $\mu_{r,\text{in}} = 2a_b$ and $\mu_{r,\text{out}} = 5a_b$.

We initialize the disk with an inclination of $i = 120^\circ$ and ascending node $\Omega = 90^\circ$ with respect to the plane of the binary. The high initial inclination ensures that the disk starts within the librating region that will evolve towards polar alignment. For test particles around an equal-mass binary, there is no difference between the choice of prograde ($i = 60^\circ$) and retrograde ($i = 120^\circ$) orbits, as the evolution of the test particle only depends on whether the angle between the binary and disk plane is greater than the critical inclination i_{crit} . When full three-body systems are considered, angular momentum can be exchanged between the binary system and the circumbinary particles (Farago & Laskar 2010; Martin & Lubow 2019). This creates a difference between the prograde and retrograde orbits, and orbits with large angular momentum ratios $j = L_{\text{disk}}/L_{\text{b}}$ can lead to the formation of “crescent” librating orbits (Chen et al. 2019; Abod et al. 2022). Since we do not model the exchange of angular momentum between the disk and the binary, we expect the prograde and retrograde cases to be similar.

We simulate the region from $1.07a_{\text{b}}$ to $10.7a_{\text{b}}$, using 144 cells in the radial domain. For simulations with $\alpha > 0.01$, the viscous timescale $t_{\text{visc}} \sim r^2/\nu$ is short enough that viscous spreading of the disk material reaches the edge of our simulation domain. For these simulations, we expand the outer radial domain to $r_{\text{out}} = 35.7a_{\text{b}}$, using 216 cells across the new radial domain.

3.2 Polar-Aligning Warped Disks

Our second set of simulations studies the effects of disk warping in a polar-aligning disk around an eccentric binary. As described in Section 2, polar-aligned disks benefit from faster

precession times due to smaller central cavities and the response from the central binary, making them ideal for studying disk breaking. Our setup here is very similar to the one used in the previous section, using an equal mass, eccentric central binary surrounded by a moderately thin disk. The orientation of the binary and disk is such that polar orientation aligns the disk to the simulation xy-plane. To better examine the presence of warps, we remove the truncation at the outer radius, allowing the disk to extend to the outer radial domain. As with Section 3.1, we vary the α -viscosity parameter between $\alpha = 10^{-1}, 10^{-2}, 10^{-3}$, and 10^{-5} . These values correspond to disks with $h/r < \alpha$ (diffusive regime), $h/r \sim \alpha$ (intermediate case), $h/r > \alpha$ (wave-like regime), as well as a case in the inviscid limit. The disk is initialized with a 60° inclination to the central binary plane and evolved for 1000 binary orbits.

3.3 GW Orionis

Our third set of simulations is made to replicate the GW Orionis system. We use the known binary parameters from Kraus et al. (2020), using the AB-C binary separation of $a_b = 8.89$ au as the system scale. Previous simulations of the GW Ori system from Smallwood et al. (2021) found that the motion of the inner AB binary provides smaller effects to the disk compared to the larger motion of the AB-C binary, so we model the GW Ori triple system as the outer binary to simplify calculations as in Section 2.3. Our binary model consists of the AB binary as one mass of $M_{AB} = 0.742M_{\text{tot}}$ and the outer C component as the second mass $M_C = 0.258M_{\text{tot}}$, placed in an orbit with semi-major axis $a_b = 8.89$ au and eccentricity $e_b = 0.379$.

We simulate the region from $1.5a_b$ to $50a_b$, covering a range of roughly 13 au to 450 au. We use 192 cells across the radial domain. The disk is given an initial inclination of 38° relative to the orbit of the outer binary. For the disk structure, we use power-law exponents of $d = 2.5$ and $s = 1.0$. This gives the disk a surface density profile of $p = 1.5$ and a constant h/r throughout, which we choose to be $(h/r)_0 = 0.075$. We truncate the inner edge of the disk at $\mu_r = 24 \text{ au} = 2.7a_b$ and use a disk viscosity of $\alpha = 10^{-5}$. We expect this simulation to be similar to the simulations of Smallwood et al. (2021) with a small inner radius, generating a break at around $10a_b$. Although the disk viscosity is lower than their simulations, we expect the inner edge of the disk to be truncated at a similar radius due to the torque of the binary and, with $\alpha < h/r$, the disk remains in the wave-like regime and should break in a similar fashion. We run these simulations for 5000 binary orbits, enough time for the inner cavity to settle and the warp to propagate through the disk. We do not attempt to reproduce the disk from the Kraus et al. (2020) simulations, due to the thin disk scale height of $h/r = 0.02$ used in their work. Resolving this disk at the required inclination would require a large increase in the overall grid resolution, which we consider prohibitively expensive.

3.4 Multiple Breaks

As described in Section 2.4, the equations for t_p and t_c suggest a disk can undergo multiple breaks if the power-law slope of t_p is less than that of t_c . This can occur given the right combination of disk geometry and density profiles. To examine this possibility, we run an additional simulation with a disk that is predicted to undergo multiple breaks by Equations

(2.6) and (2.7). To maximize the chance of multiple breaks, we choose a polar-aligning disk with steep density and temperature profiles.

We modify our setup for the polar disk simulations, changing the radial domain so the inner domain remains at $r_{\text{in}} = 1.07a_{\text{b}}$ but extending the outer radial domain to $r_{\text{out}} = 100a_{\text{b}}$ using 272 radial cells across the radial domain. We use power-law profiles of $d = 4.0$ and $s = 2.5$ ($p = 3.75$). We choose the disk scale height to be $(h/r)_{r=5a} = 0.075$. Combined with the temperature profile, the disk scale height ranges from $(h/r)_{\text{in}} = 0.251$ at the disk inner edge to $(h/r)_{\text{out}} = 0.013$ at $r = 50a_{\text{b}}$. To ensure the disk is resolved as the scale height decreases, we use a single level of mesh refinement to refine the regions between $r = [8.89a_{\text{b}}, 52.1a_{\text{b}}]$ and $\theta = [50.8^\circ, 129.1^\circ]$. The disk viscosity is set to $\alpha = 10^{-5}$, as in the nearly inviscid cases.

A disk with these parameters is predicted to undergo either two or three breaking events, depending on the exact location of the inner radius. The location of this setup is marked on each panel of Figure 2.3 with an ‘ \times ’. For the left panel, with $r_{\text{in}} = 2.5a_{\text{b}}$, the breaks are predicted to occur at distances of 4.0, 8.6, and 29.1 a_{b} . We evolve this disk for 1500 binary orbits, enough time for the outer parts of the disk to evolve for a few orbital timescales.

CHAPTER 4

VORTEX FORMATION IN POLAR DISKS

Contributing Authors: Zhaohuan Zhu (University of Nevada, Las Vegas), Rebecca Martin (University of Nevada, Las Vegas), Stephen Lubow (Space Telescope Science Institute)

4.1 Polar Alignment of the Disk

We observe polar libration of the disk in all of our simulations. Figure 4.1 shows the evolution of the disk's angular quantities over time for various values of the α -viscosity. The top two panels show the disk inclination and ascending node oscillating about $i = \Omega = 90^\circ$, with a precession time t_p that increases with disk viscosity. The third and fourth panels of Figure 4.1 show the polar libration of the disk in reference to the simulation xy-plane, using the angles θ_{polar} and Ω_{polar} , the angle between \vec{L}_{disk} and \vec{e}_b and longitude of ascending node in the xy-plane, respectively. We calculate these angles using

$$\theta_{\text{polar}} = \arccos\left(\frac{L_z}{L}\right) \quad (4.1)$$

and

$$\Omega_{\text{polar}} = \arctan\left(\frac{L_y}{L_x}\right). \quad (4.2)$$

The precession of the disk causes Ω_{polar} to circulate. As the disk oscillates, inclination damping causes the oscillation amplitude to shrink over time, allowing the disk to settle towards a polar orientation and θ_{polar} to decrease towards 0. For a disk with fixed density and temperature distributions, the timescale for polar alignment t_{align} is inversely proportional

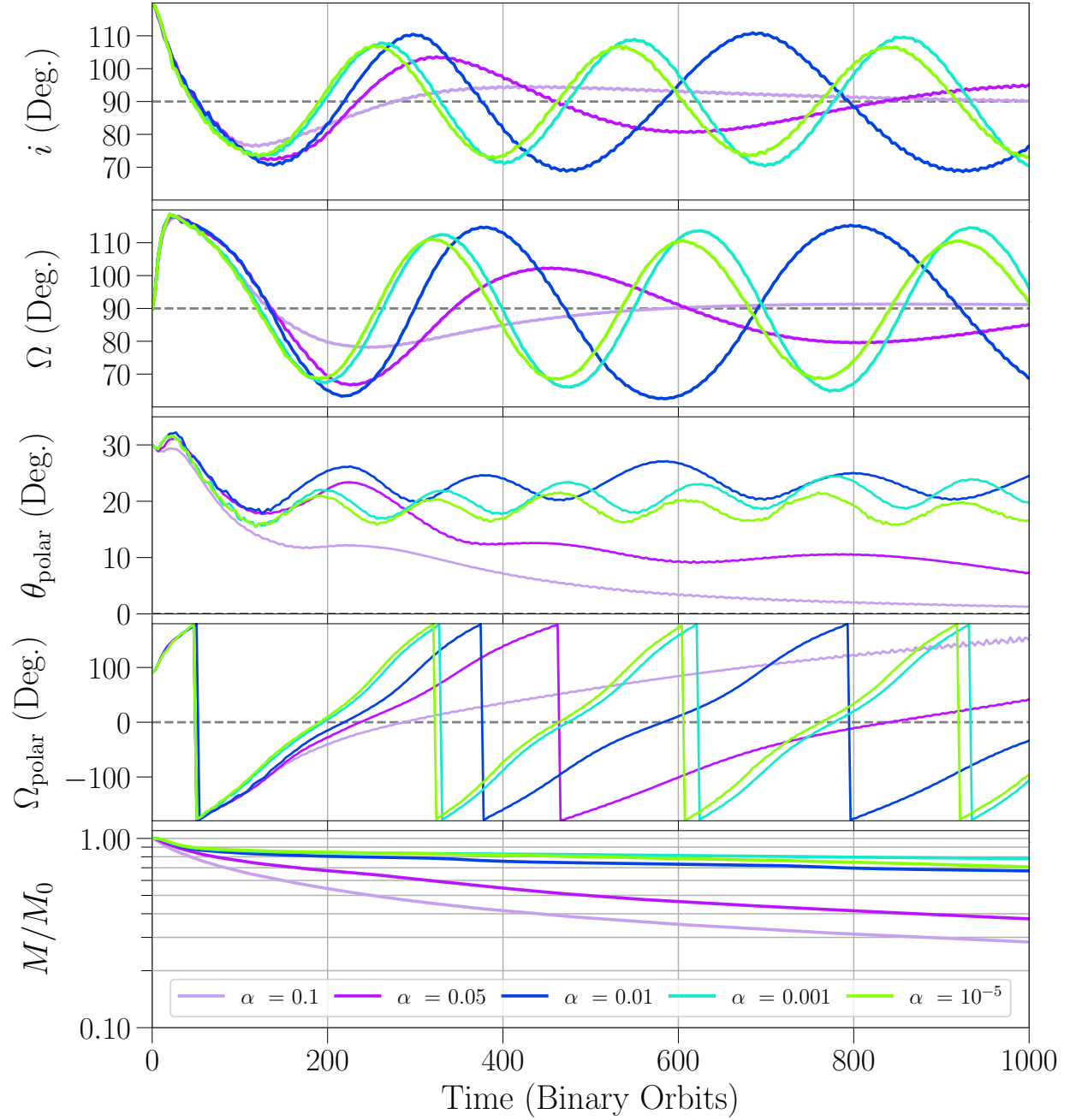


Figure 4.1: Time evolution of the disk for different values of α , showing large changes in orientation. *Top*: Disk inclination i . *Top Middle*: Longitude of ascending node Ω . *Middle*: Angle between the disk and the binary eccentricity vector θ_{polar} . *Bottom Middle*: Longitude of ascending node in the xy-plane Ω_{polar} . *Bottom*: Disk mass as a fraction of the initial mass. All angular quantities are measured in reference to the binary orbital plane at a distance of $R = 3a_b$.

to α (King et al. 2013; Lubow & Martin 2018), and so disks with a higher α -viscosity settle towards a polar alignment quicker, performing less oscillations before reaching a polar configuration.

Using Figure 4.1, we estimate polar alignment timescale to be roughly $300T_b$ for the $\alpha = 0.1$ simulation, and $500T_b$ for the $\alpha = 0.05$ simulation. This is roughly consistent with the analytic predictions given by Equations 29-30 of Lubow & Martin (2018), which give $t_{\text{align}} = 220T_b$ and $455T_b$, respectively. For simulations with $\alpha < 0.05$, the oscillation amplitude is not significantly reduced over the course of the simulation time, suggesting that the timescale for polar alignment has grown to the order of at least thousands of binary orbits. Our observed polar alignment timescales are also similar to the high-resolution SPH simulations of Martin & Lubow (2018), which use 10^6 particles. SPH simulations with a lower particle resolution show a quicker damping of the tilt oscillations and a shorter alignment timescale. Additionally, their SPH simulations which compare to the linear theory of disk warping use a disk with $i = 80^\circ$ and find that significant tilt decay occurs within 1000 binary orbits for disks with $\alpha \lesssim 0.01$.

We measure the precession periods in the $\alpha = 0.1$ and $\alpha = 0.01$ simulations to be roughly $300 - 400T_b$. The precession period increases at later times as disk material is redistributed outwards. These precession rates are in rough agreement with the SPH simulations of disks studied in Martin & Lubow (2017) and Martin & Lubow (2018) (see their Eq. 2) with the same Shakura-Sunyaev viscosity ¹, which measure precession periods of roughly $290T_b$ with initial inclinations of 80° .

¹For these SPH simulations, the equivalent artificial SPH viscosity is $\alpha_{\text{SPH}} = 4$ and 0.4 , respectively (Lodato & Price 2010).

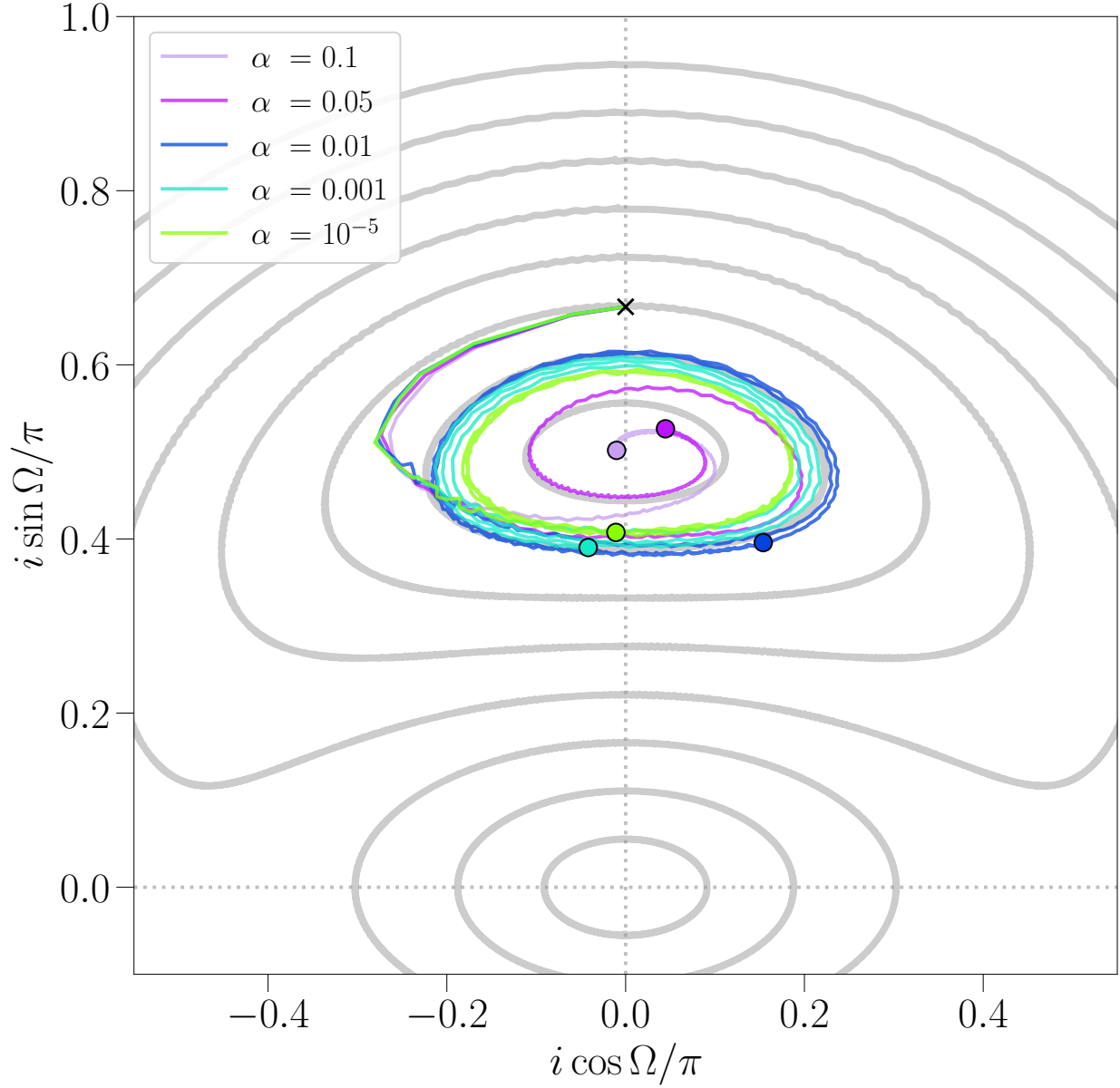


Figure 4.2: Trajectories of the simulations in $i \cos \Omega - i \sin \Omega$ phase space. Each trajectory starts at the black ‘ \times ’ and spirals inwards counterclockwise towards the point $(0.0, 0.5)$, with the final state of each simulation at 1000 binary orbits marked by the colored dots. Angular quantities are measured in reference to the binary orbital plane at a distance of $R = 3a_b$, as in Figure 4.1. Gray paths show the trajectories of test particle orbits, spaced by 10° .

Figure 4.2 plots the trajectories of the disk in $i \cos \Omega - i \sin \Omega$ phase space, along with trajectories of test particle orbits in gray. After an initial damping phase, which is present in all simulations, the disk trajectories spiral inwards towards the point $(0.0, 0.5)$, which corresponds to a disk positioned exactly perpendicular to the binary orbital plane with $i = 90^\circ$. High-viscosity disks ($\alpha \gtrsim 0.05$) quickly align towards a polar orientation, while disks with lower viscosities ($\alpha < 0.05$) follow nearly closed oscillating trajectories close to the 70° test particle trajectory, with lower α values tracing out trajectories slightly closer to a polar orientation.

Figure 4.3 shows the disk surface density profiles at $t = 1000T_b$. The inner edge of the disk drops off quickly in all simulations at roughly $2a_b$, with higher viscosity disks exhibiting a smaller inner cavity. This behavior is in agreement with previous numerical simulations (Franchini et al. 2019) and analytical predictions on the size of the disk inner cavity (Miranda & Lai 2015; Lubow & Martin 2018), which suggest that disks in a polar orientation should be truncated closer to the binary than those in a coplanar orientation. Miranda & Lai (2015) examine binary torques to determine the inner cavity size and suggest that the disks in these simulations should be truncated at the 1:3 outer Lindblad resonance. Streams of gas that flow into the central gap may carry much or all of the gas required for a steady-state accretion disk, as in the coplanar case (Artymowicz & Lubow 1996; Shi et al. 2012; Muñoz & Lai 2016).

The surface density profiles generally follow a wider, less steep distribution with increasing α -viscosity. Since the kinematic viscosity ν is proportional to α , higher viscosity disks are able to spread out further due to their shorter viscous timescale $t_{\text{visc}} \sim R^2/\nu$. As the disk material spreads out radially, the change in mass distribution increases its moment of inertia,

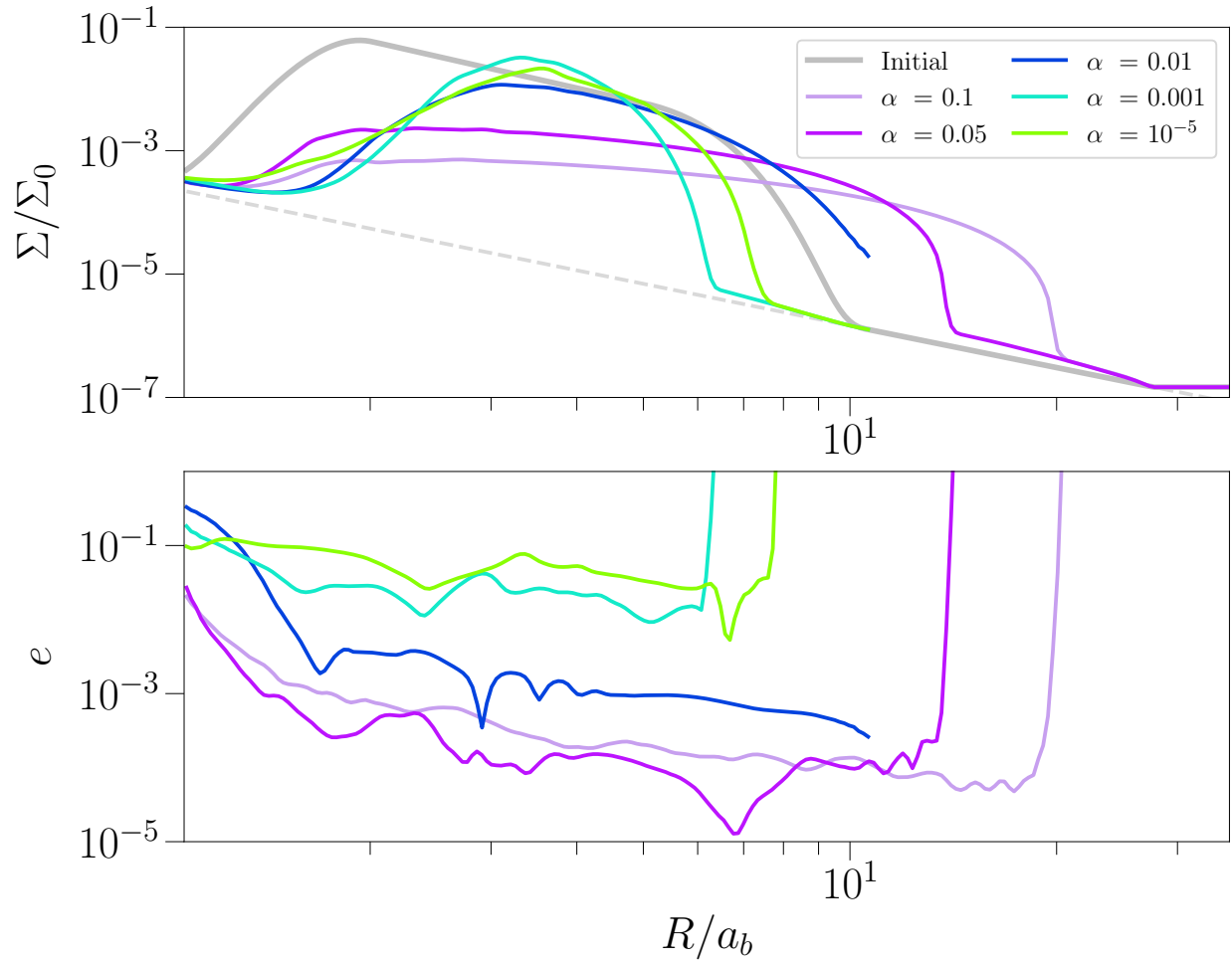


Figure 4.3: *Top*: Spherically integrated radial surface density profiles at $t = 1000$ binary orbits, plotted on a logarithmic scale. *Bottom*: Radially averaged disk eccentricity at $t = 1000$ binary orbits, calculated with Equation 16 of Shi et al. (2012).

resulting in an increase in the precession time as seen in Figure 4.1. The difference in surface density evolution between the $\alpha = 0.1$ and $\alpha = 0.01$ cases likely accounts in part for how t_{align} departs from a pure $1/\alpha$ dependence as α changes. Notably, the $\alpha = 10^{-5}$ disk does not follow this trend, instead having a slightly wider surface density profile than the $\alpha = 10^{-3}$ simulation. This may be due to the formation of vortices at low values of α , which generate spiral wakes in the disk. These spirals can increase the outward transport of material and widen the surface density profile. We discuss the details of vortex formation and its impacts on the disk in Section 4.2.

The bottom panel of Figure 4.3 shows the shell-averaged eccentricity of the disk at $t = 1000T_b$, calculated using Equation 16 of Shi et al. (2012). The disk eccentricity increases and eventually saturates over the course of the simulation, so these values can be taken as a maximum for each simulation. We find that simulations with $\alpha \gtrsim 0.01$ are able to maintain low eccentricities, while disks with lower viscosities are excited to moderate levels ($e \sim 0.1$) of eccentricity.

4.2 Formation of Anticyclonic Vortices in Low-Viscosity Disks

A gallery of disk midplane profiles is shown in Figure 4.4. As discussed in Figure 4.3, higher viscosity disks are larger and more spread out due to their shorter viscous timescale, with a lower overall surface density. Some spiral features are visible along the inner edge of the disk in all simulations, which vary in strength as the disk precesses and changes its orientation relative to the binary. Beyond this, most of the simulations support disks that remain relatively featureless.

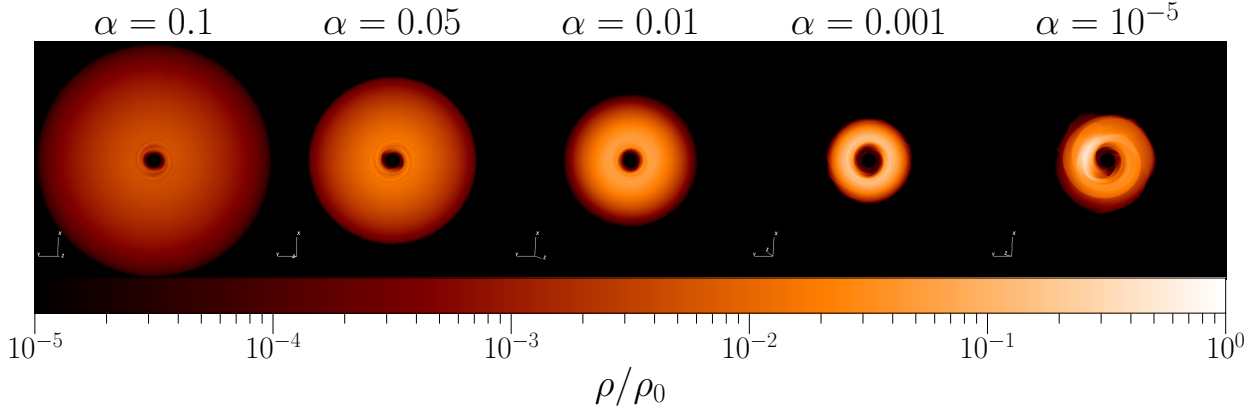


Figure 4.4: Face-on midplane density profiles of the disk at $t = 675T_b$.

The notable exception to this is the inviscid $\alpha = 10^{-5}$ simulation. This disk shows a prominent crescent-shaped density enhancement along its inner edge, as well as an associated one-armed spiral trailing away from the density feature. Horseshoe or crescent-shaped overdensity features are a known class of disk substructure and have been observed in ALMA continuum images (Casassus et al. 2013; van der Marel et al. 2013; Casassus 2016). They have previously been explained as disk material moving on eccentric orbits (Ragusa et al. 2017) or vortices generated via the Rossby Wave Instability (RWI, Lovelace et al. (1999); Li et al. (2000)). Our simulations are the first instances in which vortices are observed within polar-aligning disks. The steep drop in surface density along the inner edge of the disk creates a local minimum in the local vortensity, an important characteristic in generating the RWI (Bae et al. 2015). Vortex formation can be suppressed by a small amount of disk α -viscosity (de Val-Borro et al. 2007; Fu et al. 2014; Zhu et al. 2014; Owen & Kollmeier 2017), so it was not observed in the previous SPH simulations of polar disks.

A closeup of the overdensity feature is shown in Figure 4.5. The left and right panels show the midplane disk density and vorticity, respectively. We calculate the local disk vorticity

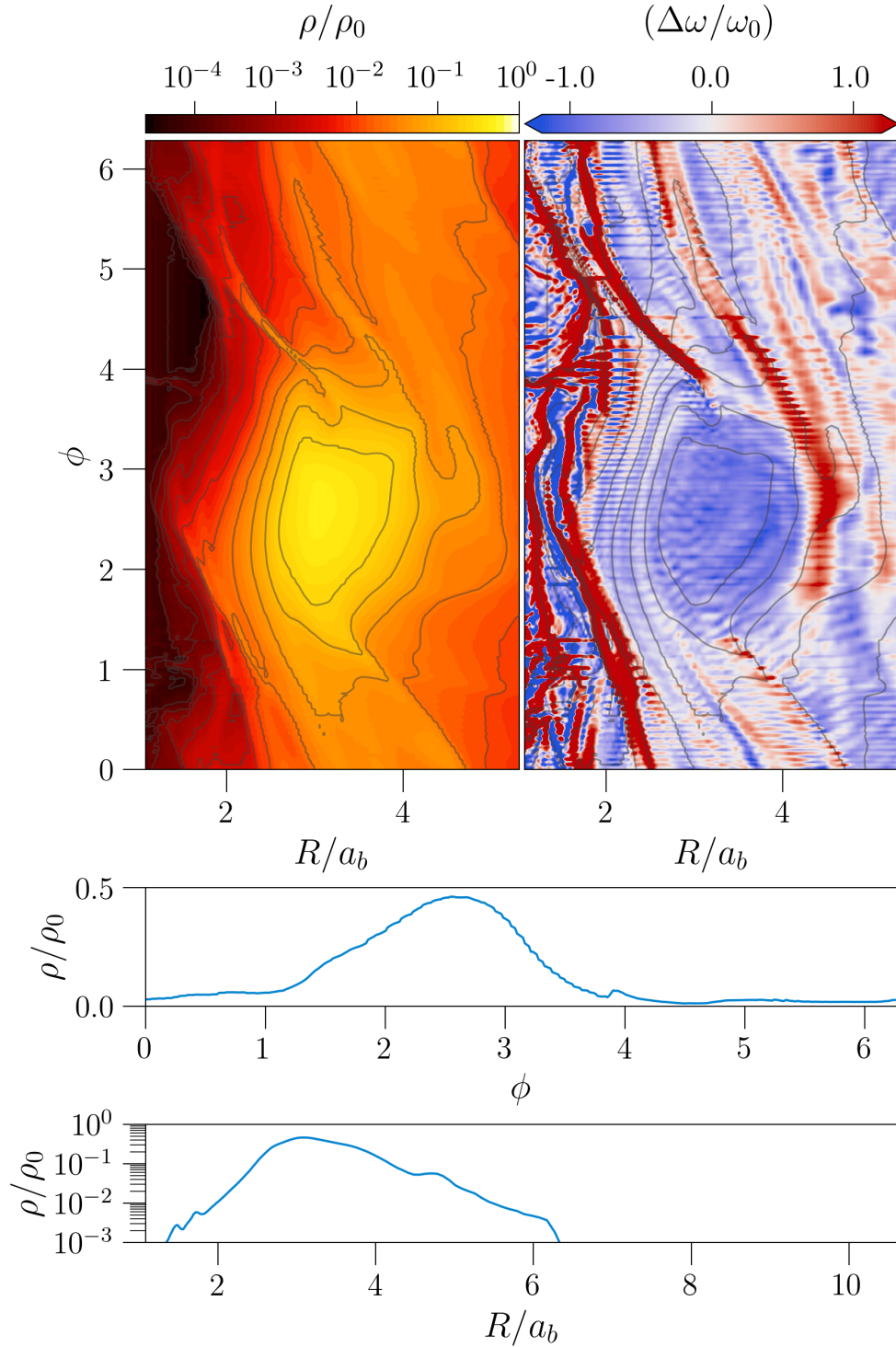


Figure 4.5: Closeup of the vortex in the $\alpha = 10^{-5}$ simulation at $t = 692$ binary orbits. *Top left:* Gas midplane density. The local overdensity and spiral arm pairs are clearly visible. *Top right:* Local vorticity. Strong anticyclonic regions are indicated in blue. Spiral arms are visible as red diagonal lines in the vicinity of the vortex. In both plots, black curves show contours of density. *Middle:* Azimuthal density across the vortex center. *Bottom:* Radial density across the vortex center.

as $(\omega - \omega_0)/\omega_0$, where $\omega = -(\nabla \times v_\theta)$ and $\omega_0 = \frac{1}{2}\Omega_K$ is the initial Keplerian vorticity. The densities and velocities at the disk midplane are calculated by transforming the disk data using the procedure outlined in the Appendix. After the coordinate transformation, the unit vector in θ at the disk midplane points downwards, opposite in direction to the local unit vector in z , so we add a negative sign to our calculation of vorticity to match the sign convention used in other coordinate systems, i.e. $\omega = \nabla \times v_z$. Large areas of anticyclonic motion are coincident with the overdense region, confirming that the crescent feature is associated with the formation of a vortex. The density cuts across the vortex (bottom two panels of Figure 4.5) show that the peak gas density ρ_{\max} is enhanced by a factor of $\gtrsim 8$ times the background, which is consistent with previous simulations of vortices generated by the RWI (Lyra et al. 2008; Bae et al. 2015).

Two spiral arms are visible on the leading side of the vortex, extending along slanted density contours and trailing inwards along the star. A similar pair of outward pointing spirals are present on the trailing side of the vortex, but are less defined, causing the two arms to combine and produce a single wide spiral arm behind the vortex. In the vorticity plot of Figure 4.5, the spiral arms appear as diagonal red lines of positive vorticity. Taken together, these form two distinct pairs of spiral arms originating from the location of the vortex; first, a “central” pair of spirals originating along the centerline of the vortex at constant R (roughly $3a_b$ in the figure), and a “tangential” pair of arms running tangent to the vortex core and originating from the inner and outer edges of the vortex relative to the disk center.

The initial triggering of the RWI and creation of the vortex in the inviscid simulation follows the evolution outlined in Bae et al. (2015). We show the time evolution of the vortex

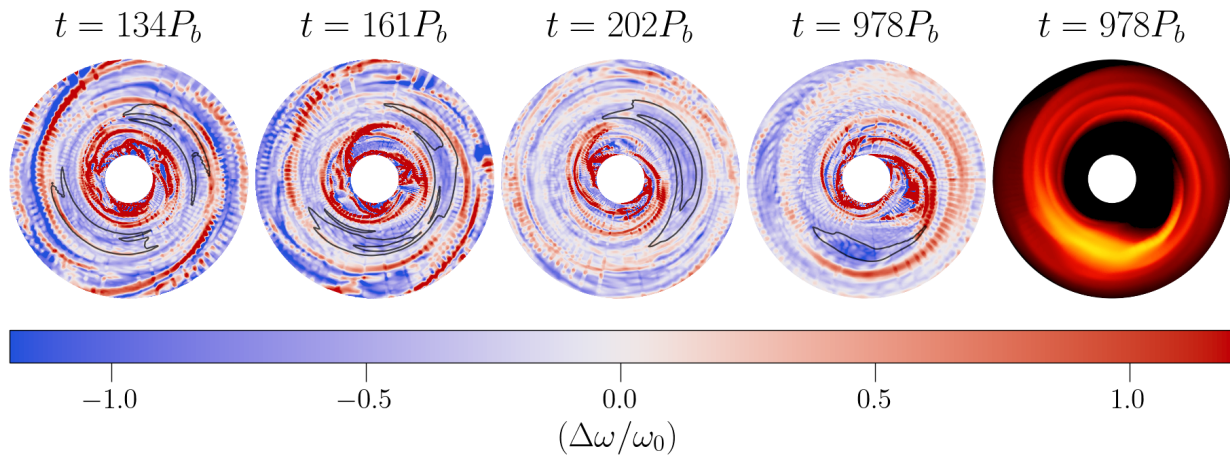


Figure 4.6: Snapshots of the $\alpha = 10^{-5}$ simulation, showing the local disk vorticity. In the left four panels, blue regions denote areas of large anticyclonic vorticity. The black contours highlight high-density regions ($\rho = 0.6\rho_{\max}$) within the disk midplane. *Far Left*: Early on, the RWI is triggered with an $m = 2$ mode, creating two vortices on opposite sides of the disk. *Left*: Differences in orbital velocities cause the vortices to move together and merge. *Middle*: The result is a single vortex which orbits at the inner edge of the disk. *Right*: The remaining vortex is long-lived, and persists until the end of the simulation. *Far Right*: Midplane disk density, showing the vortex as well as the multiple spiral arms. The density scale is shifted compared to Figure 4.5 in order to highlight the spiral arms.

growth and formation in Figure 4.6. The large vortensity minimum at the inner edge of the disk generates several RWI vortices during the linear growth phase of the instability (far left). The number of initial vortices can vary, but our simulations show a consistent $m = 2$ mode present within the first few tens of binary orbits. The appearance of this mode may be related to the presence of the central binary components, as previous studies using single stars find the $m = 3 - 5$ modes to have the fastest growth rates (Li et al. 2000; Lin 2012).

Once the initial set of vortices are formed, slight differences in their orbital speeds cause them to migrate towards each other and merge (left), resulting in a single anticyclonic vortex orbiting along the inner edge of the disk. The merging process is relatively quick, and all vortices are combined into a single vortex within a few hundred orbits of their initial creation

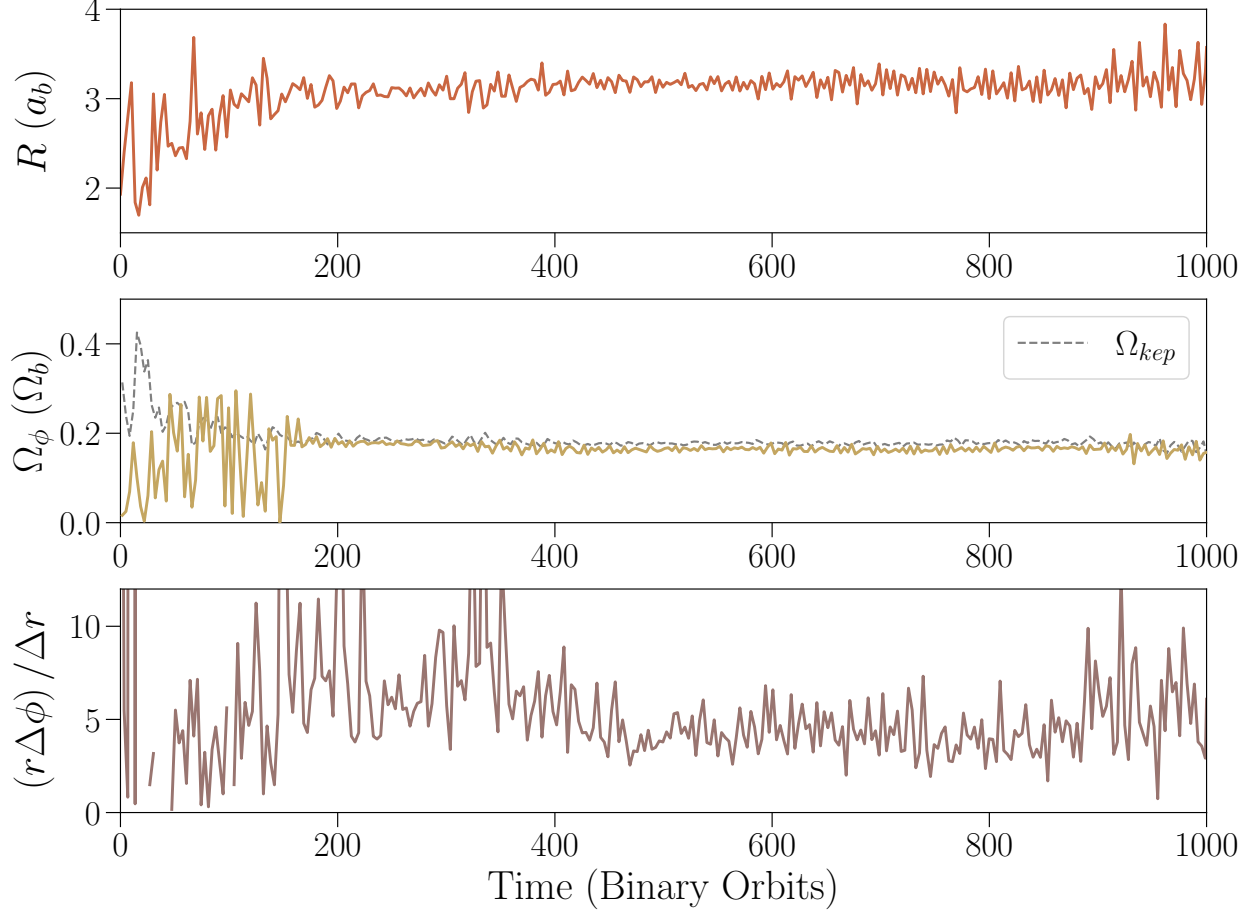


Figure 4.7: Orbital motion of the vortex in the $\alpha = 10^{-5}$ simulation. *Top*: Orbital radius of the vortex. *Middle*: Orbital frequency, in units of the binary orbital frequency Ω_b . The dotted line shows the Keplerian orbital speed at the vortex’s orbital radius. *Bottom*: Vortex aspect ratio $\chi = r\Delta\phi/\Delta r$.

(middle). The remaining single vortex persists until the end of the simulation (right). A comparison of the disk density (far right) shows the coincident overdensity and spiral arms as in Figure 4.5.

We show the orbital motion of the vortex in Figure 4.6. To locate the center of the vortex, we consider the averaged position of cells with $\rho > 0.5\rho_{\max}$ to locate the radial and azimuthal location of the vortex core. The extent of these cells across the disk allows us to calculate the vortex aspect ratio $\chi = r\Delta\phi/\Delta r$. After the initial vortices merge, the remaining single

vortex orbits at a distance of roughly 3 times the binary separation close to the Keplerian orbital speed. The aspect ratio is somewhat variable after the merger, but sits around a value of $\chi \sim 5$.

CHAPTER 5

WARPS AND BREAKS IN CIRCUMBINARY DISKS

Contributing Authors: Zhaohuan Zhu (University of Nevada, Las Vegas), Rebecca Martin (University of Nevada, Las Vegas), Stephen Lubow (Space Telescope Science Institute)

5.1 Warping and Breaking in Polar Disks

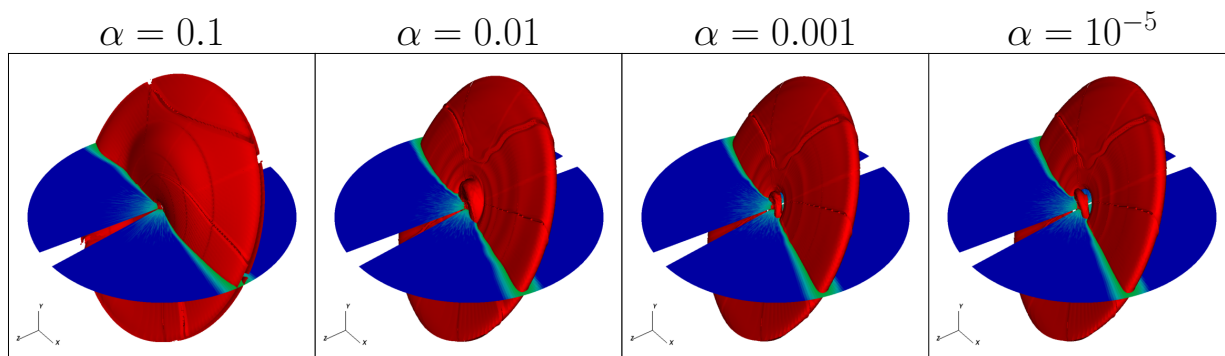


Figure 5.1: Density contours of the polar-aligning disks at $t = 1000$ binary orbits. Horizontal slice shows disk density, along the plane of the binary. Disks in the $\alpha = 0.01, 0.001,$ and 10^{-5} cases are broken; the inner disk in the $\alpha = 0.01$ simulation has momentarily reconnected with the outer disk as it precesses about the binary eccentricity vector.

Our simulations of polar disks show both wave-like and diffusive behavior, depending of the chosen value of α . Figure 5.1 shows snapshots of the various disks at $t = 1000T_b$, which display varied types of warp evolution. For the high viscosity $\alpha = 10^{-1}$ simulation, the disk develops a strong warp which evolves diffusively, while for the $\alpha = 10^{-2}, 10^{-3},$ and 10^{-5} simulations the disk breaks and exhibits bending waves. We examine the evolution of the angular momentum component l_z in Figure 5.2. In all simulations, an initial warp is

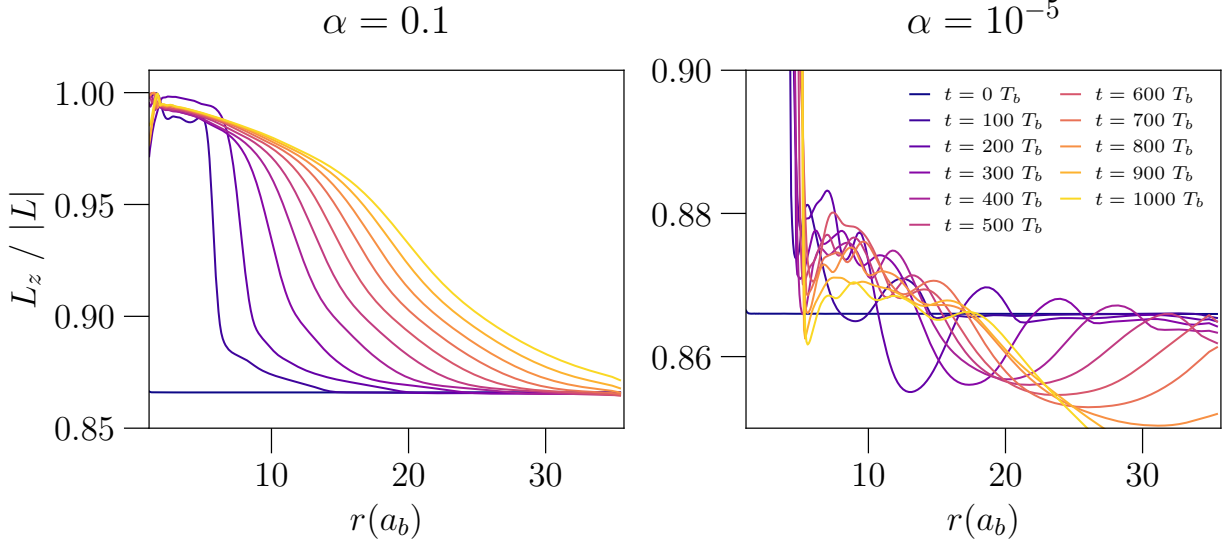


Figure 5.2: Evolution of the warp profile for the viscous ($\alpha = 0.1$, left) and inviscid cases ($\alpha = 10^{-5}$, right). Each curve represents the z -component of the unit angular momentum vector \mathbf{l}_z as a function of radius. Curves are plotted every 100 binary orbits.

excited in the disk by the central binary in the first ~ 200 binary orbits. For disks in the diffusive regime, the inner regions quickly align towards a polar orientation due to the short alignment timescale, and the initial warp slowly spreads outwards. For disks in the wave-like regime, the initial warp develops into a sharp discontinuity, a feature characteristic of a disk breaking event. External to this break, a smaller disturbance propagates throughout the outer part of the disk.

To determine the location of the warp and follow its movement within the disk, we track the position of maximum ψ as the disk evolves. In the case of a disk that breaks, two large peaks in ψ are produced, one at the breaking radius and another at the bending wave in the outer disk. We locate and track both of these peaks to follow the locations of the breaking radius and the warp in the outer disk. The warp location and propagation speed for our warp simulations is shown in Figure 5.3.

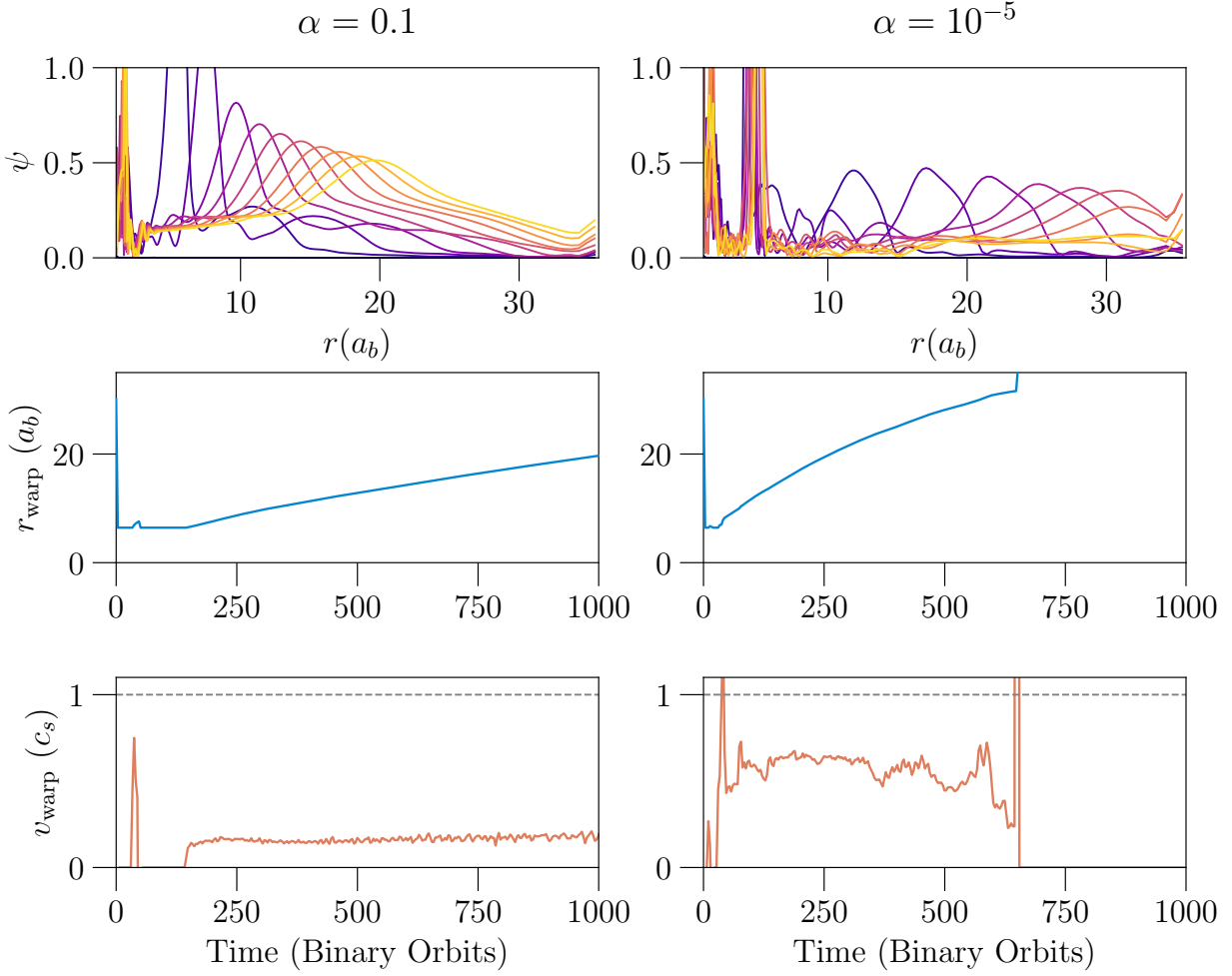


Figure 5.3: Motion of the warp for the viscous ($\alpha = 0.1$, left) and inviscid cases ($\alpha = 10^{-5}$, right). *Top row:* The ψ parameter plotted against the disk radius. Curves are plotted every 100 binary orbits as in Figure 5.2. *Middle row:* The radial location of the warp, determined as the local location of maximum ψ . For wave-like propagation, both the initial break and secondary wave propagation are plotted. *Bottom row:* The outward propagation velocity of the warp. The dotted line represents the local sound speed velocity of c_s at the warp radius.

For simulations in the diffusive regime, the inner disk generates a large warp as the disk aligns to the precession axis. The warp creates a large peak in ψ that travels outwards at roughly 0.2 times the local sound speed. The left-hand panels of Figures 5.2 and 5.3 show that the warp starts as a very steep and narrow feature, but broadens over time, encompassing a range of approximately $10a_b$ by the end of the simulation. A small wave is launched ahead of the main warp (visible in Figure 5.3 as a series of secondary purple peaks between 10 to 25 a_b , beneath the yellow curves drawn at later times). This wave does not show a corresponding feature in Figure 5.2. The diffusive nature of the disk quickly removes this wave, causing it to disappear by $t = 500T_b$.

Simulations in the wave-like regime show the disk breaking at a distance of $r_{\text{break}} = 4a_b$, with no apparent dependence on the disk viscosity. After the initial breaking event, the breaking radius slowly drifts outwards. The bottom panel of Figure 5.3 shows that the propagation speed of the bending wave decreases as it travels outwards in the disk, traveling close to one-half of the local sound speed.

We examine the drift of the breaking radius in Figure 5.4. Each panel shows the location of the breaking radius for a simulation with a particular α viscosity, with curves plotting the normalized surface density and vertical dashed lines marking the location of the breaking radius at each time. An outward drift of the break is seen for the $\alpha = 10^{-2}$ and 10^{-5} simulations, but not for the $\alpha = 10^{-3}$ simulation. For the $\alpha = 10^{-5}$ simulation, the initial break forms at roughly $r_{\text{break}} = 4.25a_b$ and slowly drifts outwards until $t = 800T_b$, where it appears to stabilize at a final location of $5.1a_b$. The $\alpha = 10^{-2}$ simulation breaks the disk slightly farther out, at $r_{\text{break}} = 4.65a_b$, and drifts outwards at a rate nearly twice as fast as the inviscid simulation. By the end of our simulation time, the break has reached a radius

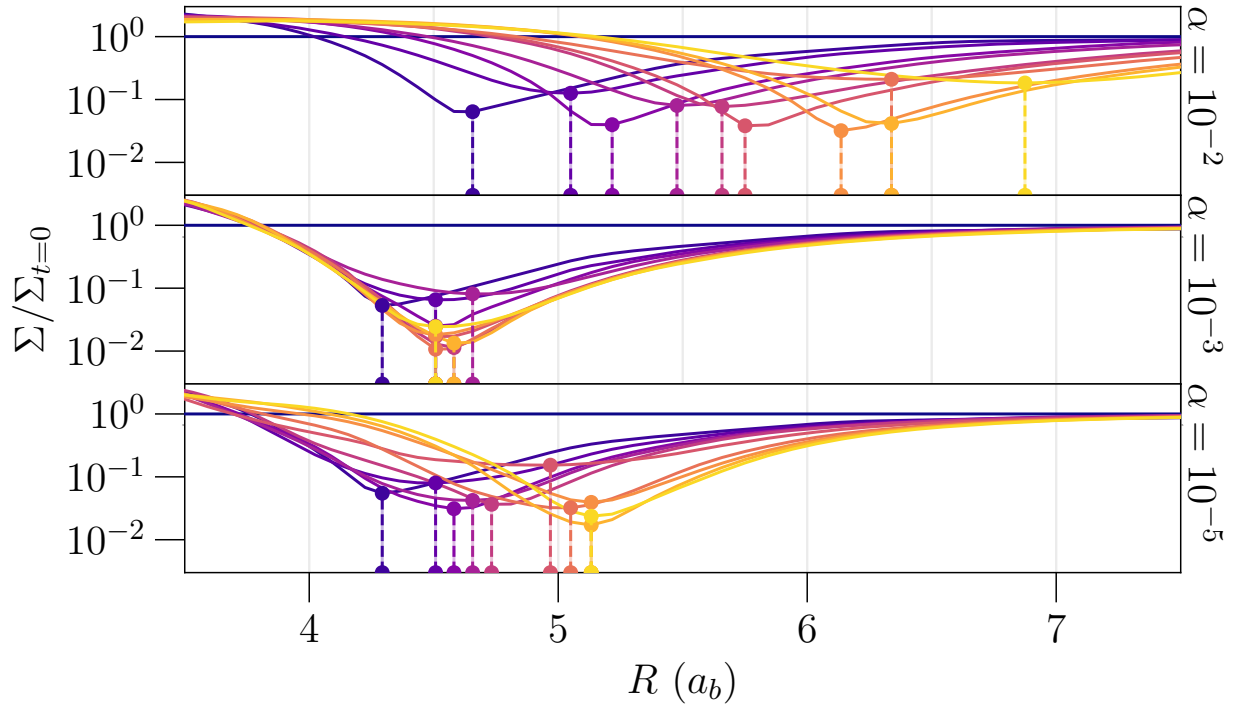


Figure 5.4: Drift of the breaking radius observed in our polar-aligning disks in the bending wave regime. Each panel shows the normalized surface density of the disk every 100 binary orbits, for different disk viscosities. Colors are the same as in Figures 5.2 and 5.3. Vertical dashed lines indicate the location of the breaking radius for each snapshot.

of $7a_b$, and does not appear to have slowed down. In both simulations, the vertical lines marking the location of the breaking radius are unevenly spaced, suggesting that the break may not be growing at a constant rate. Instead, the break may move outwards in periodic events as the inner and outer disks momentarily realign, allowing for increased accretion flows between the two disks.

Our analytical equations for disk breaking (Section 2) show close agreement with the location of the break observed in the numerical simulations. In Figure 5.5 we compare the observed location of the disk break in our $\alpha = 10^{-5}$ simulation to the location predicted by Equations 2.11 and 2.12. The breaking radius is visible as a sharp drop in the disk surface

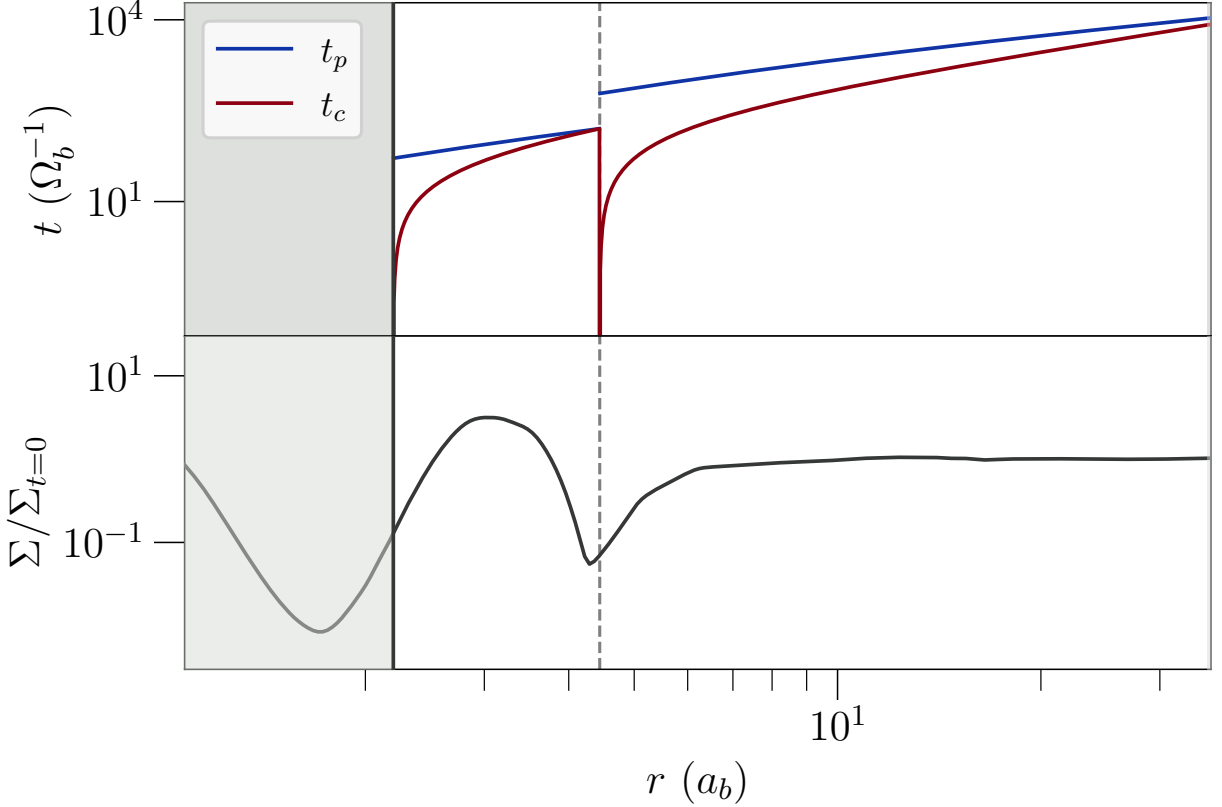


Figure 5.5: Comparison of the simulated breaking radius to analytical predictions. *Top:* Analytical timescales as predicted from Equations (2.11) and (2.12). Here, r_{in} is calculated to be $2.2a_b$ (see text for details). *Bottom:* Surface density of the $\alpha = 10^{-5}$ simulation at $t = 100$ binary orbits, in units of the initial surface density profile Σ_0 . The breaking radius is denoted by the sharp dip in Σ/Σ_0 . In both plots, vertical dashed lines indicate the predicted locations of the breaking radius.

density. We show the disk surface density at $t = 100T_b$, just after the initial break has formed. Choosing a snapshot at early times is important for an accurate comparison as the location of the break drifts outwards over time.

To determine the value of r_{in} used in our analytic equations, we compare the density-weighted angular momentum of the disk $\int \Sigma r^3 \Omega dr$ to the analytic value expected for a disk with the same surface density power law profile. For this calculation, we choose a snapshot shortly after the initialization of the disk, when the simulation has had time to equalize but

before a break has had time to open up. We consider r_{in} to be the location at which these two values diverge. For the polar-aligning disks, this gives a value of $r_{\text{in}} = 2.2a_b$.

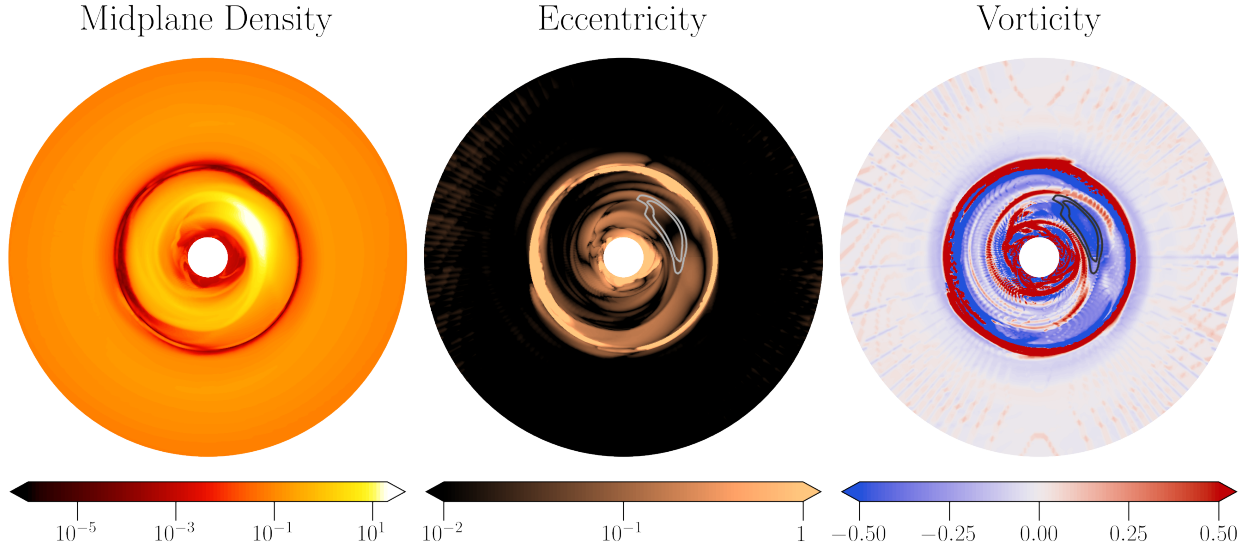


Figure 5.6: inner regions of the $\alpha = 10^{-5}$ polar-aligning simulation, projected back onto a single plane. *Left:* Midplane density. The inner disk features an RWI vortex. *Center:* Disk eccentricity. The inner disk is somewhat eccentric. *Right:* Disk vorticity. Note the strong vorticity minimum at the location of the vortex.

We also observe the creation of substructures in the individual disks created after the breaking event. Figure 5.6 shows the $\alpha = 10^{-5}$ simulation as it would appear “flattened” onto a single plane, as well as the disk eccentricity and vorticity. We calculate the local eccentricity and vorticity of the disk using similar techniques to those used in Chapter 4. With low disk viscosities, the inner disk develops a large Rossby Wave Instability (RWI) vortex, as well as a localized overdensity and a single-armed spiral. This feature is identical to the vortices seen in the polar-aligning disks of the previous chapter.

Less features are observed in the outer disk; some faint two-armed spirals are visible at

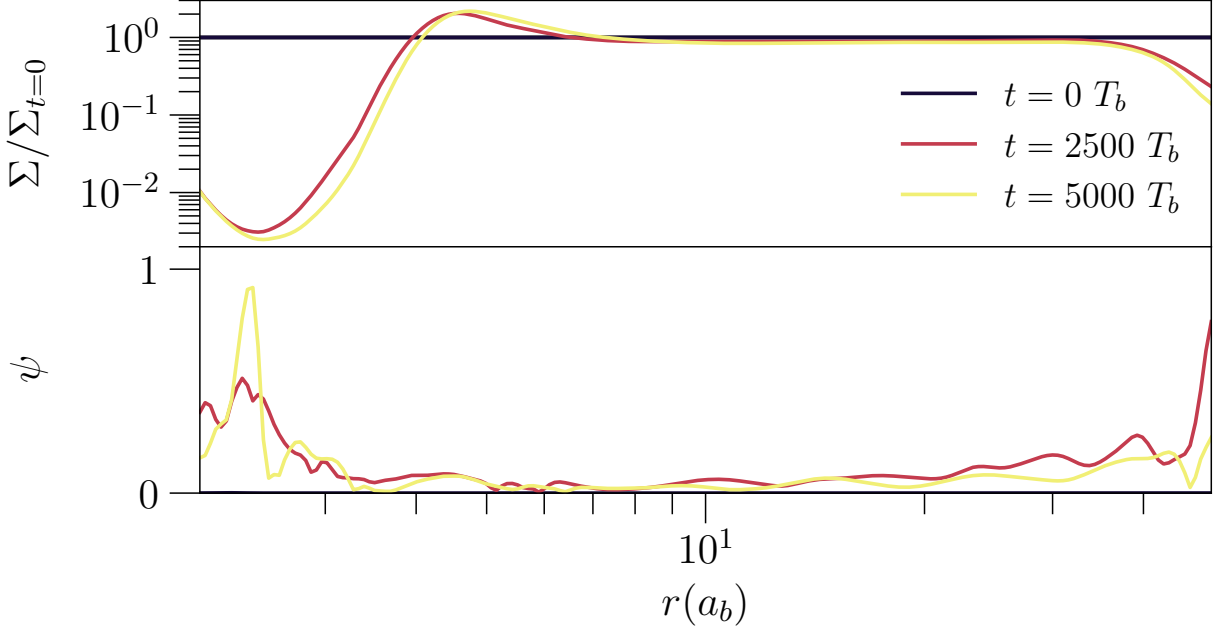


Figure 5.7: Surface density and warp profile of the GW Ori simulation at $t = 0, 2500,$ and $5000T_b$.

certain times, and no vortices are present. Simulations with a slightly higher disk viscosity, $\alpha = 10^{-3}$ or 10^{-2} , show similar details in the gap region, but have no substructures in the inner disk. We consider that the lack of vortices in the outer disk may be due to the fact that the outer disk has undergone less dynamical times, and so may not have had enough time to develop a large vortex at its inner edge. The gap depth between the inner and outer disks may also not be as steep as the inner edge of the inner disk, which is truncated by the central binary, and so may inhibit the outer disk from generating a strong vortensity minimum and growing the RWI Bae et al. (2015).

5.2 GW Orionis

Figure 5.7 shows the time evolution of the surface density and warp profile of the simulation representing the GW Orionis system (Sec. 3.3). The disk develops a mild warp within the first 1000 orbits of the outer binary. However, no disk breaking event occurs, even after the simulation is run forward for the next several thousand binary orbits. A light warp persists in the disk throughout this time, but is mostly confined to the inner regions of the disk and is never large enough to become unstable and grow into a full break. We run additional tests with different α -viscosities, running the simulation out to at least 1000 binary orbits, but none of the simulations are able to create a break in the disk.

The arrangement of the components in the GW Orionis system changes the strength of the induced binary precession. The terms in Equation 2.10 suggest that the precession induced by the binary is strongest for polar-aligning disks around high-eccentricity, equal-mass binaries. The outer binary of the GW Orionis system has a moderate binary eccentricity of $e_b = 0.379$ and a mass ratio of $q = M_C/M_{AB} = 0.348$, making the precession rate (normalized by Ω_b) of this system about one-fifth as strong as that induced by the polar-aligning disks of the previous section.

In our simulations, the binary torque truncates the inner edge of the disk at a distance of roughly $r_{\text{in}} = 3.5a_b$. This larger value of r_{in} creates a larger inner cavity than is observed in the simulations of Smallwood et al. (2021), and is larger than the value we initially used for calculating the breaking radius above. The size of the inner cavity remains larger even for runs with the same α -viscosity as the Smallwood et al. (2021) simulations. If we recalculate the location of the breaking radius with the value of r_{in} observed in the simulations, the disk

timescales change such that no break is expected to occur in the disk.

5.3 Multiple Disk Breaking

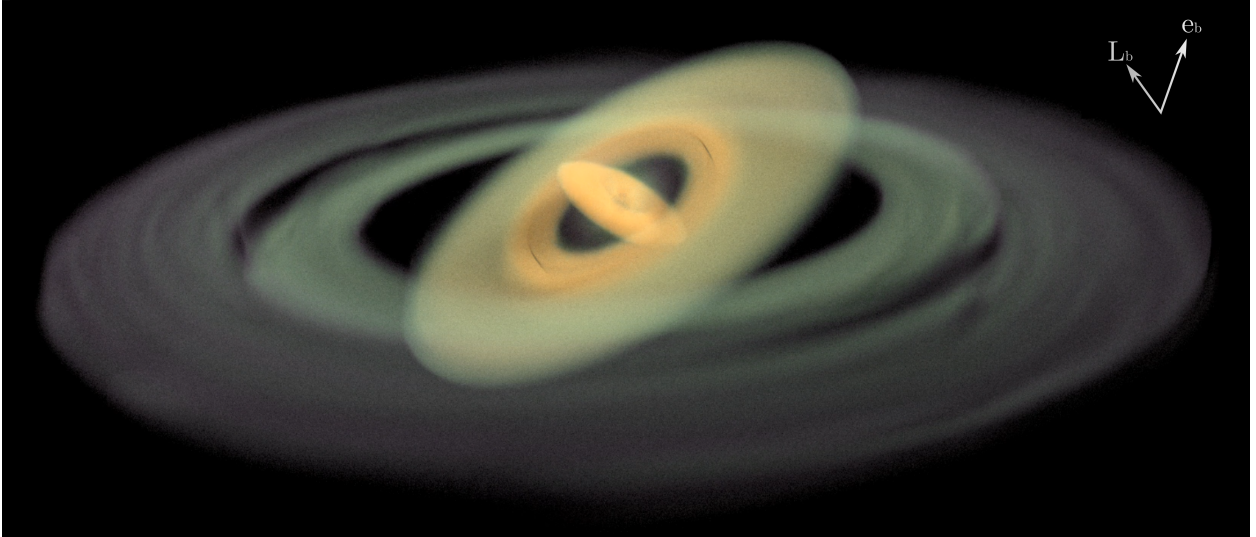


Figure 5.8: Rendering of the multiple break simulation at $t = 1200$ binary orbits. The directions of \mathbf{L}_b and \mathbf{e}_b are indicated in the top right, with \mathbf{L}_b pointing into the page. The first two breaks at $7a_b$ and $28a_b$ are visible. There is a large warp at $35a_b$ that appears similar to a break, but the disk is not broken at this distance. See text for details.

A visualization of our multiple break simulation (Sec. 5.3) is shown in Figure 5.8. Two disk breaking events are visible, separating the disk into three distinct rings. At the end of the simulation, the disk breaks are located at radial distances of 7 and $28a_b$, with the outer edge of the disk reaching equilibrium at roughly $r_{\text{out}} = 60a_b$. The third ring shows a strong warp at roughly $35a_b$. This warp is strong enough for the disk to appear broken due to how thin the disk is at this radius, but subsequent analysis will show that the disk is still communicating across the apparent gap. Similar to the polar disks in Section 5.1, we see RWI vortices form in the innermost disk, but not in the second or third disks.

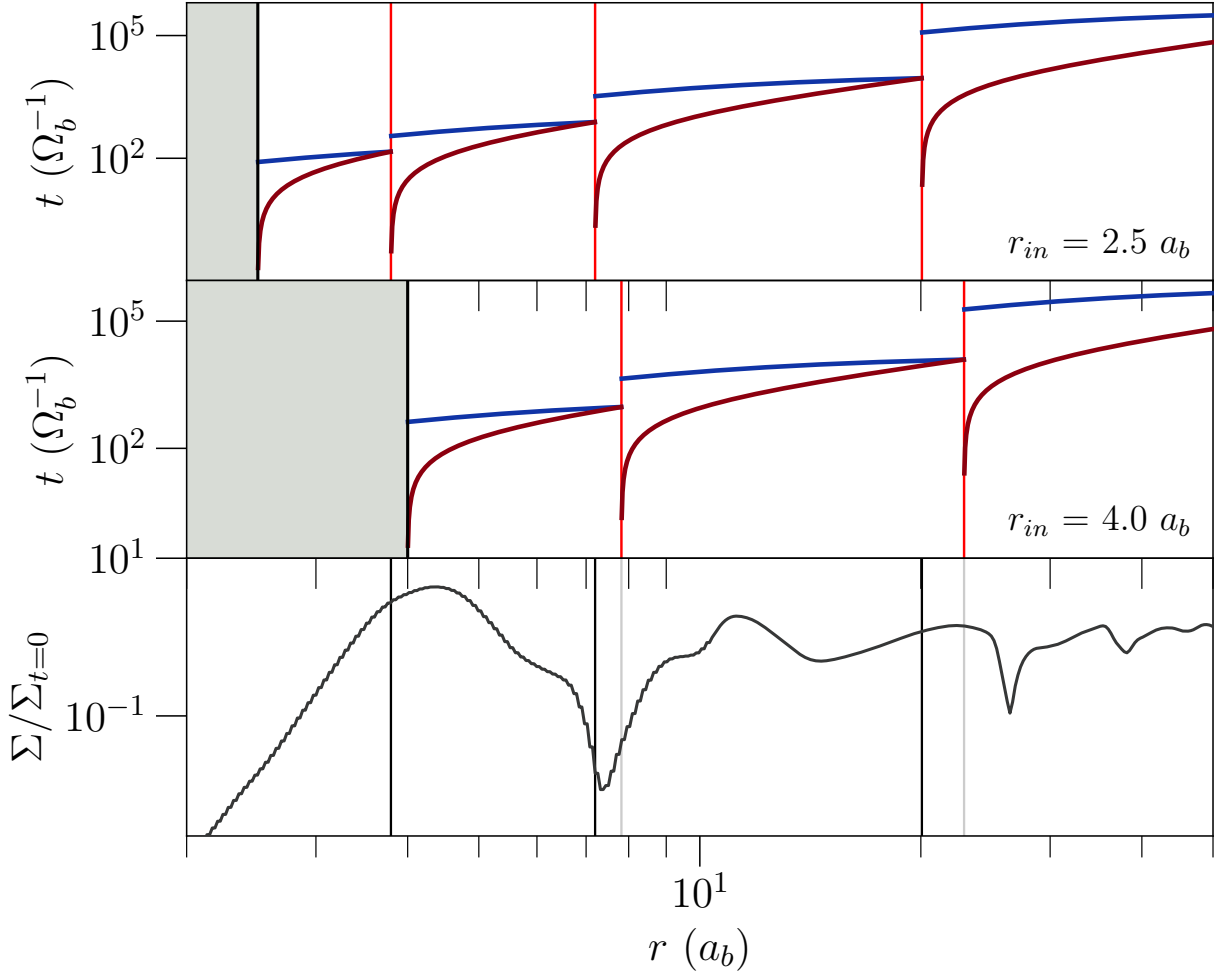


Figure 5.9: Similar to Figure 5.5, but for the multiple break simulation. In this figure, each panel shows different choices of the inner radius, $r_{\text{in}} = 2.5a_b$ (top) and $r_{\text{in}} = 4.0a_b$ (middle). Both choices produce outer breaking locations that are roughly consistent with the observed breaks in the simulation. The bottom panel is from a simulation at a time of $1500T_b$.

Figure 5.5 compares the observed locations of each break to the locations predicted by the timescale equations. We find it is difficult to determine a suitable inner radius for this disk. Choosing an inner radius of $r_{\text{in}} = 2.5a_b$, our analytical equations predict 3 breaks, with the second and third breaks in rough agreement with the locations of the observed breaks in the simulation. The first break, expected at $r = 4.25a_b$, is not observed in the innermost disk.

If instead we try to fit the first two breaks to the observed locations, we find that the size of the inner cavity must be chosen as $r_{\text{in}} = 4.0a_{\text{b}}$ (Figure 5.5, middle panel). However, the predicted size of the inner cavity is larger than the observed size of the cavity in the simulation; in fact, the local surface density at the proposed inner edge is actually higher than the initial condition.

To better identify the regions of the disk that are in radial communication, we calculate the azimuthal angle of the shell-averaged angular momentum vector, defined as

$$\phi_L = \arctan\left(\frac{L_y}{L_x}\right), \quad (5.1)$$

In our multiple break simulation, the simulation z direction is along the binary eccentricity vector and the binary orbit is in the $x - z$ plane, so ϕ_L can be viewed as the longitude of ascending node of the disk in the $x - y$ plane as it circulates around the binary eccentricity vector. Regions of the disk in radial communication will precess together, and thus have the same value of ϕ_L . In Figure 5.10, we plot the value of ϕ_L across the disk as a function of radius and simulation time. As the disk evolves and breaks off rings, distinct horizontal bands of color emerge in the figure, each band corresponding to a separate disk in the final simulation. Disk breaking events are visible as sharp boundaries between two horizontal bands, as the value of L changes sharply from one disk to another.

In Figure 5.10, it can be seen that the innermost disk breaks off almost immediately, in about 100 binary orbits. The fast precession of the inner disk causes ϕ_L to cycle several times during the rest of the simulation, creating a colored band at the bottom of the figure. The outer disk then develops a warp that gradually extends out to roughly $25a_{\text{b}}$, before

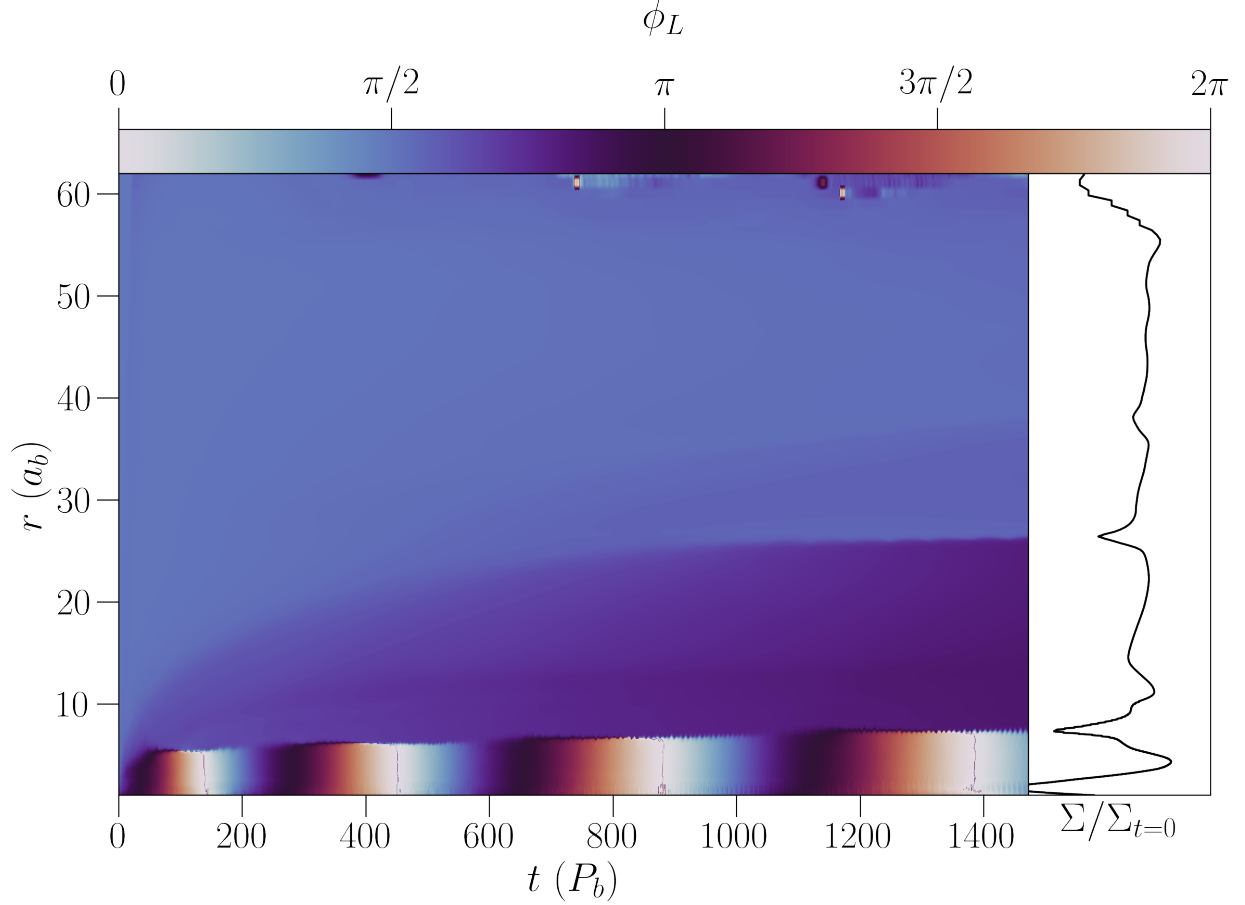


Figure 5.10: Azimuthal rotation angle plotted as a function of radial location and time. Areas in the same connected disk precess together, and create a band of the same color. By the end of the simulation, three distinct bands are visible, corresponding to the three disks in the simulation. The disk surface density profile at $t = 1500T_b$ (same as Figure 5.9) is also shown at right to compare the locations of the observed gaps.

breaking off a second disk at $1000T_b$. After the disk breaks at $25a_b$, the warp between the first and second breaks gradually vanishes as the second disk becomes coplanar. This is another indication that the disk has lost communication at the breaking radius as the outer disk cannot torque the inner disk any more. In the third, outermost disk, a faint band can be seen extending from the second break to about $35a_b$, signifying a strong warp. However, a strong discontinuity in ϕ_L has not yet formed, so this band is not yet considered a third

breaking event.

The multiple break simulation showcases the difficulty in using Equations (2.11) and (2.12) to predict the exact location of the breaking radii when multiple breaks are packed together in a small radial range. Breaking events require a few local dynamical timescales to fully develop, so the innermost break will have time to drift outwards while subsequent breaks form and develop. The bottom panel of Figure 5.9 shows that the surface density, normalized to an initial power-law distribution, is quite disturbed even in regions far away from the breaks, suggesting that the disk no longer follows a power-law distribution even though the analytic equations assume one when calculating the location of a break. We discuss this behavior further in Section 6.3.

CHAPTER 6

DISCUSSION

Contributing Authors: Zhaohuan Zhu (University of Nevada, Las Vegas), Rebecca Martin (University of Nevada, Las Vegas), Stephen Lubow (Space Telescope Science Institute)

In this chapter we discuss different aspects of the simulations, as well as their potential impacts on planet formation in circumbinary systems.

6.1 The effect of vortices vs. lumps in the disk

The overdensity feature observed in the $\alpha = 10^{-5}$ simulation behaves differently than similar features that are created in coplanar circumbinary disks. Several coplanar disks have been found to exhibit crescent or horseshoe-shaped features, but these features have been explained as a density “lump” created by gas on eccentric orbits at the inner edge of the disk interacting with streamers inflowing towards the binary (Shi et al. 2012; Miranda et al. 2017; Ragusa et al. 2017, 2020). In contrast, the overdensity feature observed in our polar disk simulations corresponds to a vorticity minimum, and is closer in nature to vortex-induced clumps created at the edges of gaps opened by massive planets (de Val-Borro et al. 2007; Zhu et al. 2014; Hammer et al. 2017).

Overdensities in circumbinary disks can drive periodic accretion onto the central binary. Simulations of coplanar circumbinary disks including the central binary components by Muñoz & Lai (2016) show the density lump causing pulsed accretion at the rate of the lump’s local orbital period. When the effects of the binary eccentricity are included, the ac-

cretion flows are pulsed at the rate of the binary orbital period, and can preferentially accrete onto one star for several hundred orbits. In Miranda et al. (2017), mass accretion around circular binaries is found to vary on short timescales of $\frac{1}{2}T_b$, as well as longer timescales of roughly $5T_b$.

Accretion rates around polar-aligned disks have been less studied. Smallwood et al. (2022) perform simulations of the HD 98800 system and find no periodicity in the binary accretion rate, instead observing a roughly constant level of accretion for a polar disk with $\alpha = 0.01$. The high viscosity in these simulations means that no vortices form in the disk, even during the passage of the outer AaAb binary.

The vortex in our inviscid polar disk produces a variable accretion rate with similar short and long-term behavior as the lumps seen in coplanar disks. In Figure 6.1 we show the shell-averaged radial mass flux in the disk over a period of roughly 10 binary orbits. Long-period flows are present at distances of $3 - 4a_b$, with an oscillation period of roughly $5T_b$. This low frequency mass flux is due to the orbital motion of the vortex around the binary, carrying the overdensity on an eccentric orbit at the local orbital frequency (Figures 4.3, 4.7). Closer to the binary, at roughly $2a_b$, we observe short-term outflows with a periodicity of roughly T_b . These outflows are caused by small streams of material pulled from the inner edge of the disk and flung outwards by the binary torque, similar in nature to those seen by Shi et al. (2012). Since our inner binary is eccentric, the streams do not pile up and form an overdense lump (Miranda et al. 2017). Overall, the vortex that appears in our polar circumbinary disks differs from the density lump in coplanar circumbinary disks in two ways: 1) the vortex only forms when α is very low, while the lump can form in disks with a much higher α (even in MHD simulations with $\alpha \sim 0.1$, Shi et al. (2012)); 2) the vortex appears in polar-aligning

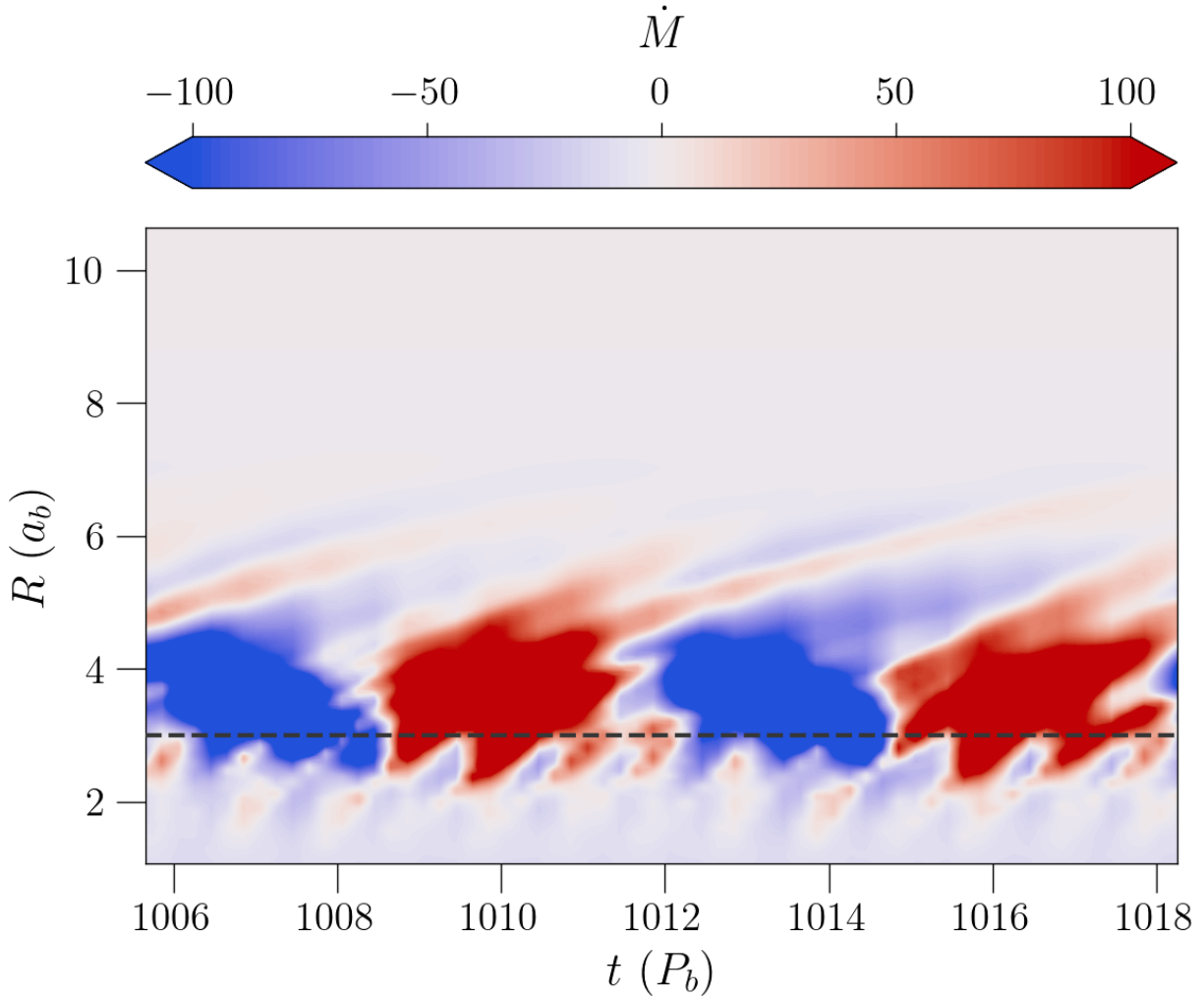


Figure 6.1: Shell-averaged radial mass flux of the $\alpha = 10^{-5}$ simulation. The dashed line marks the approximate orbital distance of the vortex. Short-period outflows are visible close to the binary ($2a_b$) as thin red stripes. Long-period variability, associated with the orbital period of the vortex, is visible from $3 - 4a_b$ as alternating red and blue bands.

circumbinary disks with an eccentric central binary, whereas the density lump only forms when the binary is nearly circular ($e_b \lesssim 0.05$, Miranda et al. (2017)).

The overdensity created by the vortex changes the local pressure gradient on the neighboring gas, producing regions of super-Keplerian and sub-Keplerian rotation just inside and outside of the vortex’s orbital radius (Kuznetsova et al. 2022). These deviations from Keplerian orbital velocity may be observable as a kinematic signature (Boehler et al. 2021), which are inverted in sign but similar in strength to the signatures formed in the gaps of protoplanetary disks, which are thought to be formed by young planets (Teague et al. 2018, 2019; Izquierdo et al. 2022). Future high-resolution studies with ALMA may be able to distinguish vortex creation in polar disks.

Observations of HD 98800 B from Kennedy et al. (2019) show a uniform disk in both gas and dust observations, with no evidence of a large scale disk asymmetry. The absence of vortex-like features may be a sign that the viscosity in HD 98800 B is high enough to prevent vortices from forming. Another explanation could be that the vortices are relatively transient features in the disk. The lifetime of vortices in the disk is on the order of thousands of orbital periods (Zhu & Stone 2014; Hammer et al. 2021). For HD 98800 B, this corresponds to a lifetime of $\lesssim 1000$ years for a vortex formed at the inner edge of the disk, which is much shorter than the disk lifetime of ~ 10 Myr (Barrado Y Navascués 2006). Therefore, it is possible that any vortices that initially formed in the disk have long since dispersed, unless they are continuously generated by the inner binary.

The rightmost panel of Figure 4.6 shows the vortex and spiral arms as they appear in the disk. The appearance of the spiral arms resembles the scattered light images of HD 142527 (Avenhaus et al. 2014, 2017), which is also known to have an overdensity feature (Casassus

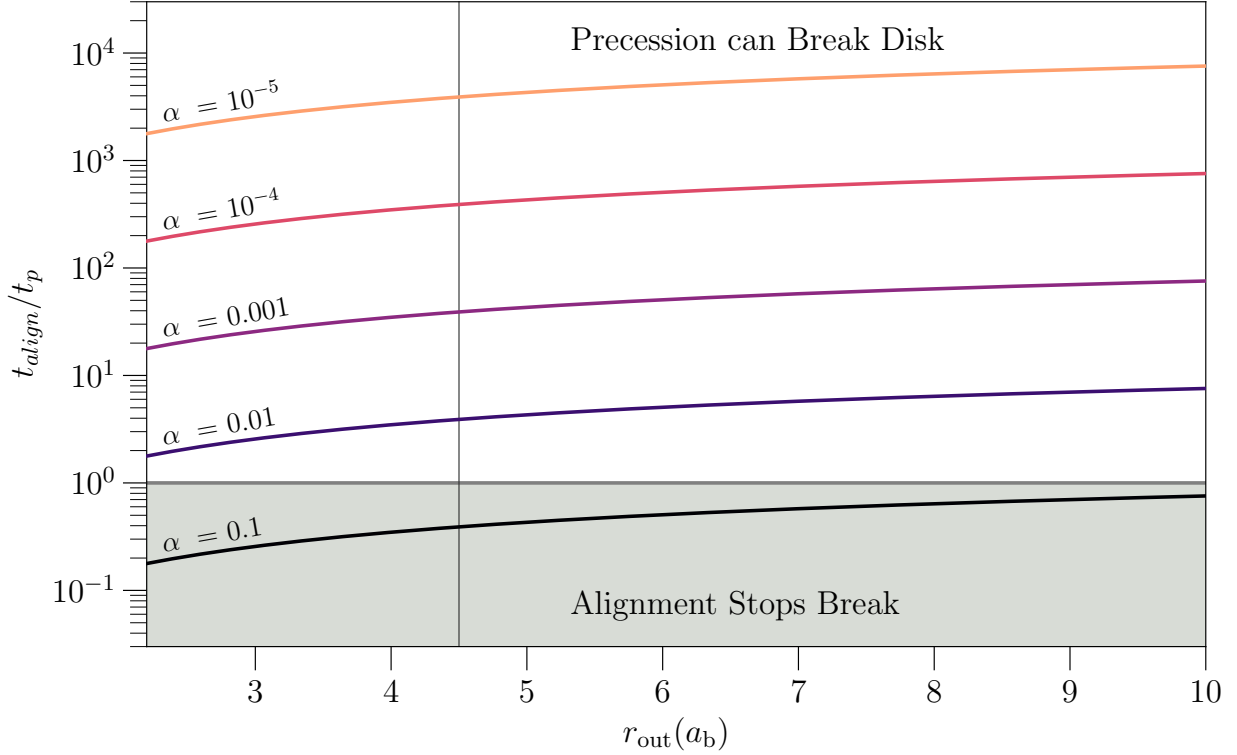


Figure 6.2: $\tau = t_{\text{align}}/t_p$ as calculated by Equation (2.14) for different values of α . The vertical line indicates the rough location of the break as seen in our low viscosity simulations.

et al. 2013). Spirals along the inner edge of the disk can also be created without a vortex due to the gravitational interaction of the binary with the disk (Price et al. 2018), so it is unclear if vortex-generated spirals are the cause of the spiral arms in the HD 142527 disk.

6.2 Viscosity in Warped Disks

We can observe the effects of disk viscosity on the polar disks in Section 3.1 by examining the value of $\tau = t_{\text{align}}/t_p$ across the simulations. We plot τ as a function of radius in Figure 6.2, with the assumption that while calculating t_p all material interior to r is able to precess coherently. We see that for our selected disk parameters, the disks with $\alpha \lesssim 0.01$ maintain $\tau > 1$ for the entirety of the disk and thus are able to break under the induced precession of

the binary.

For our $\alpha = 0.1$ simulation, we can estimate the values of the warp viscosities ν_2 and ν_3 using Figures 4 and 5 of Ogilvie (1999). From our Figure 5.3, the maximum warp amplitude is roughly $\psi_{\max} = 0.5 - 0.75$, at a distance of $r = 10a_b$. This corresponds to warp viscosities of $\nu_2 = 0.019a_b^2\Omega_b$, $\nu_3 = 0.0013a_b^2\Omega_b$, and $t_{\nu_2} = 5000\Omega_b^{-1}$.

We note that, for the simulations in Section 5.1, there is a change in the overall disk orientation of about 5 to 10 degrees from its initial orientation. This change occurs faster than the local precession timescale induced by the binary, and instead occurs as the warp (diffusive or wave-like) propagates through the disk. This effect is partially visible in Figure 5.1, since the disk, initialized in alignment with the simulation x -axis, is now misaligned at the end of the simulation. We consider this to be an effect of the ν_3 warp viscosity, which has caused the entire disk to precess.

6.3 Efficacy of the Disk Breaking Equations

The number and location of the breaking radii determined by Equations 2.11 and 2.12 is a sensitive function of the disk parameters, in particular the size of the inner cavity r_{in} . Because of this sensitivity, small adjustments in the value of r_{in} result in large changes to the predicted breaking radius. Conversely, small adjustments in the location of the breaking radii only require minor changes in the required value of r_{in} . An important caveat of this behavior is that it easily allows our description of disk breaking to remain consistent with observed disks, but it is harder for these same equations to act as predictive tools. For example, Equations (2.11) and (2.12) can be made consistent with simulations or observations by finely

adjusting the disk parameters to match the observed location(s) of the breaking radius, but it is more difficult to predict the location of emergent breaks when starting from the initial disk conditions.

When examining our polar disk simulations in Section 5.1, we initially find the expected breaking radii are different from our initial guess as the inner radius shifts and reaches a quasi-steady state. Once we adjust the value of r_{in} to account for this change, the predicted breaks are in much closer agreement. For the multiple break simulation (Section 5.3), we have a harder time trying to match both the observed breaking locations and the location of the inner radius simultaneously, especially when multiple breaks are packed in a small radial range.

The nature of this sensitivity leads to some difficulty in using Equations (2.11) and (2.12) to predict the location of disk breaks. There is no clear location at which the gas at the inner radius of the disk acts as an “edge” and stops precessing as a solid body with the rest of the disk. Thus, different methods of calculating the inner radius such as using surface density cutoffs, precession rates, angular momentum deviations, or other methods will result in slightly different values of r_{in} , leading to greatly differing estimates of the breaking radii in the disk. Differences in r_{in} caused by code formulation, such as those which may affect the GW Orionis simulations in Section 5.2, can further complicate this issue. This behavior was also noted in the simulations by Young et al. (2023), who comment that the wide dependence on disk and binary parameters make the creation of a disk breaking equation a challenging matter.

Our analytic equations are also restricted by their lack of full coverage of the possible parameters. Previous SPH simulations have observed a dependence of disk breaking with

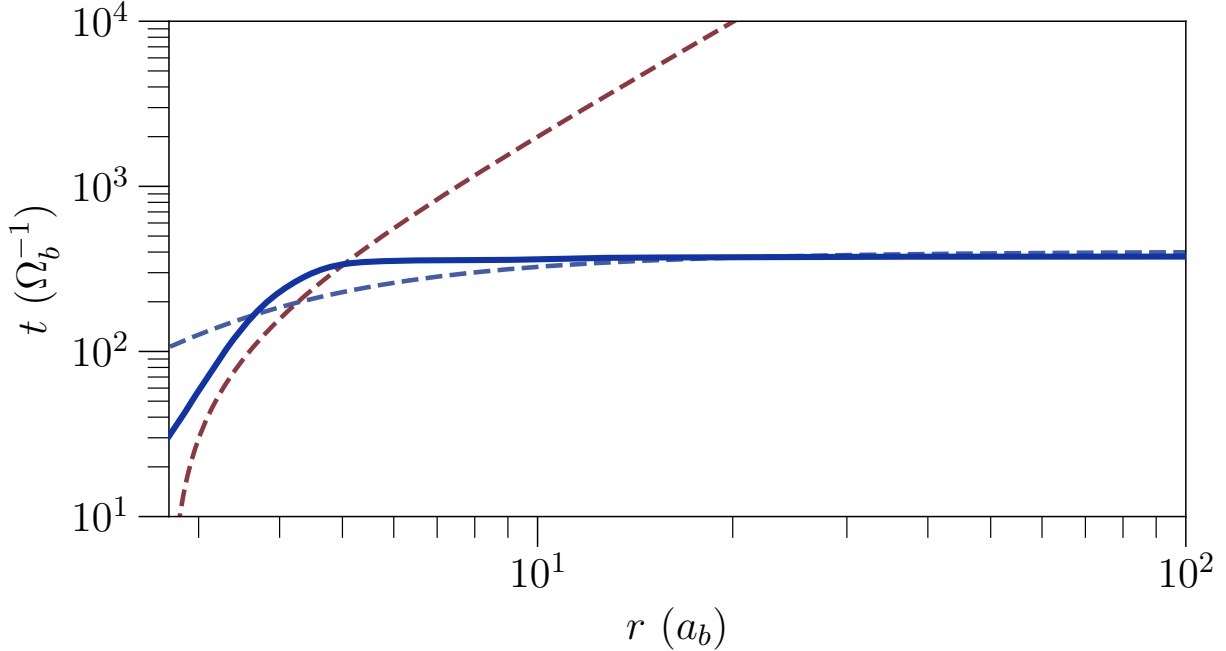


Figure 6.3: Comparison of disk timescales using the analytic equations Eq. (2.11) and (2.12) to the precession time calculated by directly integrating Eq. (2.9) with the observed surface density. Dashed red and blue lines indicate the analytic solutions for t_c and t_p , while the solid blue line shows the directly integrated value for t_p .

inclination to the precession vector (Facchini et al. 2013; Nealon et al. 2015), suggesting that disk breaks are more likely for highly inclined or retrograde disks, and may not occur if the mutual inclination between the disk and precession vectors (prograde or retrograde) is small. Analysis by Doğan et al. (2018) and Raj et al. (2021) suggest that a warp may continue to grow unstably if the warp amplitude ψ is beyond a critical limit ψ_c , a value which is dependent on the disk viscosity. The current analysis is relatively simple and is strictly analytic, using the initial power-law profiles set at the beginning of the simulation to calculate the breaking radius. As the binary-disk system evolves, the gas may settle towards different power-law profiles than those set by the initial conditions, or towards a radial distribution not approximated by a power-law profile, as seen in Figure 5.9. An example of this is shown

in Figure 6.3, where we compare the analytic, power-law disk timescales in our multiple break simulation to the timescales calculated by directly integrating Equation 2.9 (since our simulations are nearly isothermal, direct integration for t_c is identical to the analytic result of Eq. (2.12)). There is a slight outward shift in the location of the breaking radius in this case, but the new location is similar to the location predicted by the analytic equations. However, this adjustment may lead to cascading outward shifts for the subsequent breaks farther out in the disk.

We can estimate the effects of the disk inclination on our results by examining the analytic equations of Farago & Laskar (2010) describing the orbits of test particles around eccentric binaries. For a circumbinary test particle, the precession period of the particle is given in Equation (2.32) of Farago & Laskar (2010) as

$$T = \frac{16}{3n_1} \frac{M_{01}}{\beta_1} \left(\frac{a_2}{a_1} \right)^{7/2} \frac{K(k^2)(1 - e_2^2)^2}{\sqrt{(1 - e_1^2)(h + 4e_1^2)}}. \quad (6.1)$$

where n_1 , M_{01} , and β_1 are the mean motion, total mass, and reduced mass of the binary ($n_1 = 1$, $M_{01} = M_{\text{tot}}$ in our paper), and the orbital elements a_1, e_1 and a_2, e_2 refer to the semi-major axis and eccentricity of the binary and particle, respectively. The constant $h = -4e_1^2 + \sin^2 i(1 + 4e_1^2)$ describes the orientation of the test particle's orbit, and $K(k^2)$ is an elliptic integral of the first kind integrated over the azimuthal angle ϕ , defined as

$$K(k^2) = \begin{cases} \int_0^{\pi/2} \frac{1}{1 - k^2 \sin^2 \phi} d\phi & k^2 < 1 \\ \int_0^{\phi_0} \frac{1}{1 - k^2 \sin^2 \phi} d\phi & k^2 > 1 \end{cases} \quad (6.2)$$

where $k^2 = \frac{5e_1^2}{1 - e_1^2} \cot^2 i$ and $\phi_0 = \arcsin(1/k)$. The dependence of K and h on the

inclination angle causes the value of T to vary with changing inclination.

The effects of the change in precession time are shown as a function of disk inclination in Figure 6.4 for the polar-aligning setup in Section 5.1 and the GW Orionis setup in Section 5.2. The precession time lengthens considerably only in the vicinity of the critical inclination, and so we consider the effect on our simulations to be relatively small. Importantly, Figure 6.4 shows that for disks within a few degrees of the critical inclination the disk will precess very slowly and is therefore unlikely to break. Simultaneously, inclinations close to 0° or 90° are also unlikely to break, since they are aligned close to their precession vectors and will not produce a strong warp amplitude. Thus, certain inclinations between 0° and i_{crit} or i_{crit} and 90° are the most likely orientations for disk breaking.

The dependence on inclination derived here is different than that expected from Nixon et al. (2013), who predict that breaking is most efficient for inclination angles between $45^\circ < i < 135^\circ$ and is strongest at 45° and 135° . This criterion is made by considering the cancellation of angular momentum from counter-aligned rings produced as the inner disk precesses. Although this range of inclination angles is correct when considering circular binaries and Lense-Thirring precession induced from black holes, the addition of librating orbits for eccentric central binaries produces new regions at potentially moderate inclinations where disk breaking is unlikely.

6.4 Observational Signatures of Warped Disks

The changing orientation of warped disks is known to produce specific observable signatures. Warping changes the projection of the disk onto the sky plane, and produces twisted

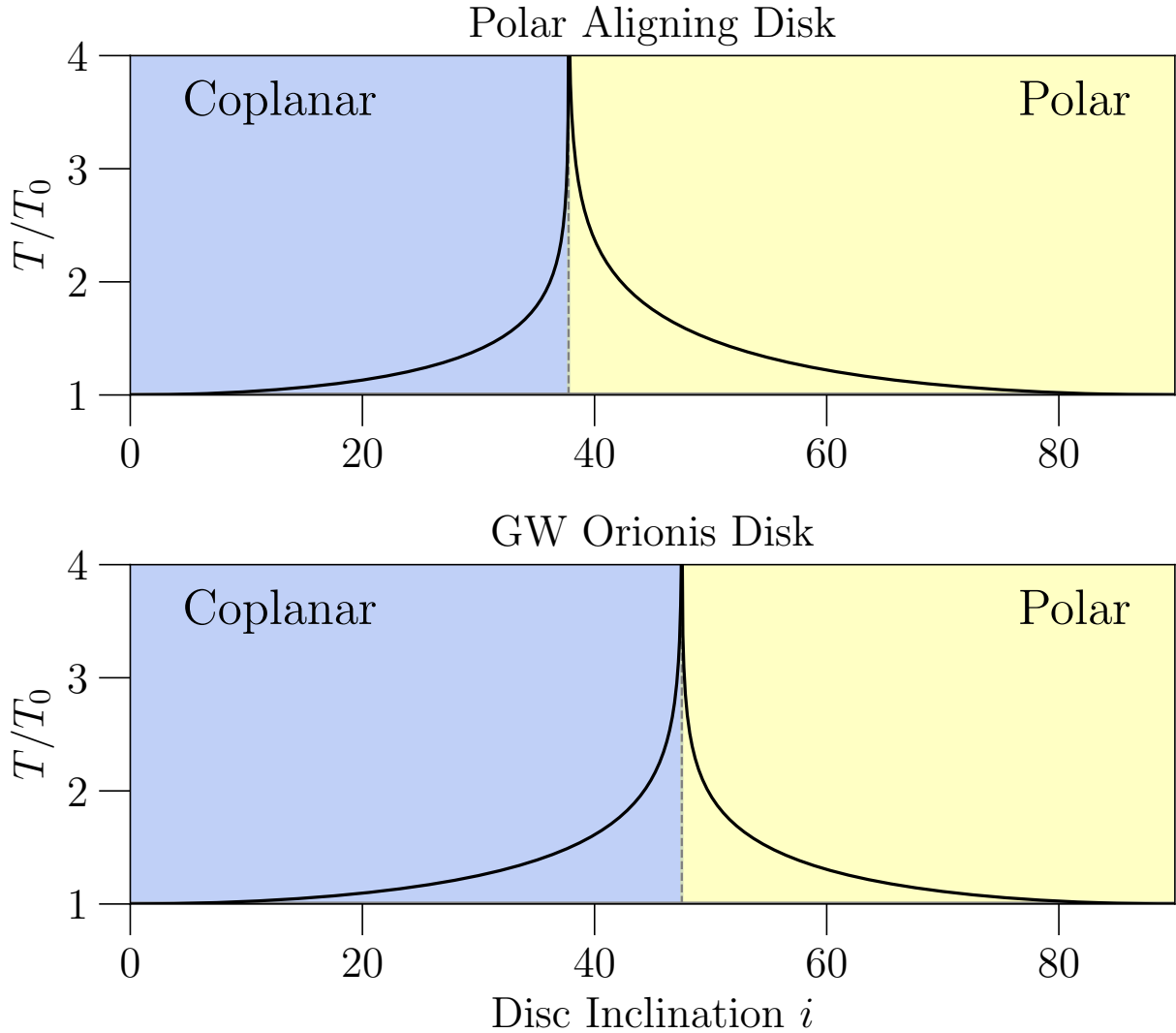


Figure 6.4: Analytic precession rates calculated from Eq. (2.32) of Farago & Laskar (2010) as a function of disk inclination, for the cases of the polar-aligning disks in Sec.5.1 (top) and the GW Ori system in Sec.5.2 (bottom). The vertical line denotes the critical inclination i_{crit} for this system; inclinations lower than i_{crit} align to a coplanar orientation, while inclinations higher than i_{crit} align to a polar orientation. Precession rates are normalized to T_0 , the precession rate for a nearly coplanar or nearly polar disk.

or S-shaped contours when viewed in molecular lines. This feature has been observed in the GW Orionis circumtriple system (Bi et al. 2020; Kraus et al. 2020) as well as within the cavities of some transition disks such as HD 142527 (Casassus et al. 2015), and can be reproduced using simulations of warped disks (Juhász & Facchini 2017; Smallwood et al. 2021). Channel maps can also explore details about the larger surrounding structures around a warped disk, and reveal if an observed warp is caused by a central source such as a binary or if the warp is related to infalling matter from the surrounding molecular cloud. In the case of GW Orionis, the identification of at least one streamer connected to the disk indicates that both effects may be at play (Czekala et al. 2017; Fang et al. 2017). High resolution kinematics of warped disks may be used to examine radial flows between broken disks and determine the strength of a disk warp, including if an observed warp is also a break.

Similar observational signatures can be found in broken disks. If the inner and outer disks are in different orientations, each disk will have differently oriented and possibly separated butterfly patterns in CO channel maps (Zhu 2019). The inner disk will cast shadows as a pair of dark lanes onto the outer disk. The orientation of these lanes may not be symmetric around the disk, and their pattern speed around the disk may not follow the precession rate of the inner disk, depending on the relative orientations of the inner disk, outer disk, and binary (Facchini et al. 2018; Zhu 2019). Disks with multiple breaks may exhibit a complex series of shadowing features, as each disk will cast shadows onto all of the disks outside of it. However, Facchini et al. (2018) find that the flaring geometry of the disk is an important feature for producing asymmetric illumination of the outer disk when the inner and outer disks have a low relative inclination. Since multiple disk breaking is less favored for flaring disks, the shadowing patterns from these disks may appear more symmetric. The

local temperature changes caused by these shadows can generate spiral arms in the outer disk (Montesinos et al. 2016), so the thermal effects of these lanes may be important when attempting to reproduce observations.

The long-term movement of these shadows can give insights to the orientation of the central disk relative to the binary. From Equation (2.10), disks in coplanar and polar orientations have opposite signs of k , and will precess in opposite directions compared to their precession axis. Long-term monitoring of circumbinary disks, combined with rotational information from kinematic observations, can be used to determine the direction of the shadow's movement, and thus the precession direction of the inner disk. This can be used to determine whether the inner disk is in a coplanar or polar configuration, and can place constraints on the arrangement of the central binary.

6.5 Prospects for Circumbinary Planets

It is currently unknown if planets are able to form within polar disks. Currently, no planets have been observed in polar orbits around binaries, nor have planet candidates been found in polar-aligned disks. The lack of detections is partially due to a strong observational bias; current methods for detecting exoplanets rely on identifying signals with multiple, periodic transits, which favors planets around single stars or circumbinary planets in coplanar alignments. Planets on circumbinary orbits exhibit large transit timing variations on the order of hours or days, orders of magnitude larger than those around single stars (Armstrong et al. 2013), which complicates their detectability. A circumbinary planet on an inclined orbit is more likely to produce single or irregularly spaced transits due to the orbital precession of

the binary torque (Martin & Triaud 2014; Chen et al. 2019, 2022), rendering most traditional detection methods unusable and requiring the use of specialized transit folding methods (e.g. Martin & Fabrycky 2021). If circumbinary planets are equally likely to form in polar disks as they are in coplanar disks, they may be as common as planets around single-star systems (Armstrong et al. 2014; Martin & Triaud 2014).

The formation of vortices within low-viscosity disks can have significant effects on planet formation history. A current problem in planet formation involves the formation of large planetary embryos in a disk, as gas drag from the disk causes growing particles to rapidly spiral inwards onto the star, before they are able to decouple from the gas (Weidenschilling 1977). Anticyclonic vortices in a disk act as local grain traps, and can intercept over half of the inward migrating grains that cross its orbit (Fromang & Nelson 2005). Once captured in the vortex, the local vorticity focuses particles towards the vortex “eye”, which can facilitate accelerated growth of planetary material all the way up to Jupiter-mass planets (Klahr & Bodenheimer 2006; Lyra et al. 2008; Zhu & Stone 2014; Owen & Kollmeier 2017). In polar disks, vortices may lead to direct planet formation or seed the disk with a large initial planetesimal population, which can allow further growth and formation of planets in polar orbits (Childs & Martin 2021, 2022).

Figures 4.5 and 4.7 show that the vortex orbits at a few times the binary separation, close to the inner edge of the disk. The sharp surface density profile created at the inner cavity wall allows the RWI to readily produce vortices in the absence of viscosity. The orbital radius for these vortices is close to the theoretical stability limit for circumbinary planets (Dvorak 1986). Curiously, many of the circumbinary planets discovered by *Kepler* and the *Transiting Exoplanet Survey Satellite (TESS)* have orbits just outside the stability limit

(Martin & Triaud 2014; Welsh et al. 2014). Taken together, this may suggest a potential *in-situ* formation scenario for close-in circumbinary planets, where the sharp inner cavity of the circumbinary disk generates long-lived vortices allowing for efficient trapping of solid materials. Rapid planet formation at this location would produce circumbinary planets close to the circumbinary inner stability limit.

CHAPTER 7

CONCLUSIONS

In this work, we have studied the behavior of misaligned astrophysical disks around a central binary, primarily in the context of protoplanetary disks during early star formation, using numerical simulations. Our use of a grid-based numerical scheme allows us to investigate previously unexplored regimes in high detail. We observe new phenomena at low disk viscosity and are able to extend previous formulations into the low-viscosity regime. We present a summary of our results below.

This work outlines the first grid-based simulations of polar-aligning circumbinary disks. We find that the disks align towards a polar orientation, with evolutionary timescales in rough agreement of the previous SPH simulations and analytic estimates. In low viscosity simulations, RWI vortices can be generated close to the inner edge of the disk while polar alignment occurs. These vortices create localized overdensities within a polar disk, and can persist for thousands of orbits. We observe two pairs of spiral arms originating from the vortex, along the center of and tangent to the vortex core. The overdensities created by these vortices are fundamentally different from similar features generated through eccentricity excitation within the disk, which is more commonly seen in coplanar disks. The combination of vortices and spiral arms may create a detectable observational signature in polar-aligning disks, although none have been observed yet. The presence of vortices and overdensities in polar circumbinary disks may also aid in the formation of polar circumbinary planets, accelerating planet growth in regions close to the circumbinary stability limit.

We also consider the behavior of warped disks in the context of circumbinary proto-

planetary disks during early star formation. Our grid-based code reproduces the previously known behaviors for warped disks in the viscous and inviscid cases, and disk breaking is readily achieved for disks in the bending-wave regime, $\alpha \lesssim h/r$. From this, we propose a viscous criterion for disk breaking, where the disk must undergo significant precession before aligning perpendicular to the precession axis in order to break.

We also derive new analytic formulations of the disk timescales in order to predict the location where a disk will break. Our formulation for disk breaking suggests that breaking events are more likely when the disk is thinner, the inner cavity is smaller, and the disk power-law profiles are steeper. These criteria are well supported by the results of our simulations, and the predicted location for the breaking radius is in agreement with the location of the breaks observed in our simulations. We show that repeated disk breaking, previously seen in simulations of AGN disks, is predicted by our analytic formulae, though it is unlikely to occur in a protoplanetary disk.

When compared against our simulations, the analytic equations produce breaking radii that are consistent with the observed locations of the breaks. However, the sensitivity of the analytic equations makes it difficult to utilize these equations in a predictive manner and precisely determine the location of the breaking radius. We have also applied our formulation to the GW Orionis system to explain the discrepancies between previous simulations and their observed breaks, though better observational constraints are required to accurately assess whether the disk will break under the influence of the binary alone.

Our simulations primarily focus on moderately eccentric binaries ($e \sim 0.5$) with equal to moderate mass ratios, and as such we have explored only a small area of the total parameter space for disk breaking. Many characteristics of the larger parameter space, such as regions

where a break spontaneously forms in the middle of the disk (Section 2.3), have yet to be fully studied. In the future, well-constrained disk parameters from observations may be combined with our analytic formulations to determine the breaking radii of warped disks.

APPENDIX

Simulations of disks are usually oriented so that the local coordinates of the disk are aligned with the axes of the simulation domain. This alignment simplifies the analysis of the simulation data, such as azimuthal slicing of the data along the disk midplane, or calculation of vorticity along the disk’s vertical axis. For grid-based simulations, aligning the fluid motion with the coordinate axes of the grid cells can help reduce numerical errors.

For disks that are inclined, warped, or precess over time, their orientation will not always be aligned with the simulation axes, and so the same quantities are harder to calculate without some prior manipulation. Here, we show our method of manipulating the simulation data of an inclined disk so that it may be analyzed in the same way as a flat, zero-inclination disk. As in the main text, we use spherical-polar coordinates for this section, but the general process can be adapted for use in any coordinate system.

Consider a disk that is inclined to the simulation axes at an angle i . Any point in 3D space can be described with *simulation coordinates* (r, θ, ϕ) or *disk coordinates* (r, θ', ϕ') , which are in general not the same. The transformation between these two coordinate systems is given by the equations

$$\sin^2 \theta' = (\sin \theta \cos \phi)^2 + (\sin \theta \sin \phi \sin i + \cos \theta \sin i)^2 \tag{A1}$$

and

$$\tan \phi' = \frac{\sin \theta \sin \phi \cos i + \cos \theta \sin i}{\sin \theta \cos \phi}. \tag{A2}$$

Equation A1 is equivalent to Equation (44) of Zhu (2019). As the equation only gives

$\sin^2 \theta'$, there is a degeneracy when trying to map coordinates on the top and bottom halves of the sphere. Therefore, we calculate $\cos \theta' = \sqrt{1 - \sin^2 \theta'}$ and multiply the value by -1 if the original polar angle θ lies below the equator of the mapped coordinates, $\theta' > \pi/2$. This condition corresponds to

$$\theta = \frac{\pi}{2} - \tan^{-1}(\tan i \sin \phi). \quad (\text{A3})$$

To construct a data fields for an untilted disk, we start by creating an evenly spaced grid along the disk coordinates θ' and ϕ' . For each grid cell, we transform the grid coordinates to simulation coordinates, locate the nearest data cell in the original simulation coordinates, and copy that cell data from the simulation into the grid cell. The result is a data cube oriented along the disk axes, which can be analyzed using traditional methods.

For velocity, additional transformations must be done to account for the rotation of the velocity components. The azimuthal distance element in the disk coordinates $d\phi'$ can be expressed in terms of the simulation coordinates as

$$d\phi'^2 = (rd\theta)^2 + (r \sin \theta d\phi)^2. \quad (\text{A4})$$

This allows us to calculate the local angle ψ between the disk and simulation grids as

$$\tan \psi = \frac{d\theta}{\sin \theta d\phi}. \quad (\text{A5})$$

In practice, we calculate ψ by comparing adjacent cells in the disk coordinates and converting back to the simulation coordinates, allowing the distances to be calculated using

a simple difference method. Once the local rotation angle is found, the velocity in the disk coordinates v'_θ and v'_ϕ can be calculated with

$$v'_\theta = v_\theta \cos \psi - v_\phi \sin \psi \quad (\text{A6})$$

and

$$v'_\phi = v_\theta \sin \psi + v_\phi \cos \psi. \quad (\text{A7})$$

As a pure rotation, the radial velocity remains unchanged, i.e. $v'_r = v_r$.

Figure A.1 shows an example of this transformation applied to a 2D spherical slice of our inclined disk setup at $t = 0$, using the system's initial inclination of $i = 60^\circ$. The transformed density and velocity (right column) are similar to that of a flat disk aligned with the coordinate system. Small artifacts are visible in regions close to the poles of the simulations due to a lack of initial data in these regions. The transformed data also exhibits some artifacts in the form of vertical striping, which arises from the nearest neighbor interpolation method applied while converting data to disk coordinates.

For simulations in this work, we transform the disk data using the total angular momentum vector $\vec{\mathbf{L}}$ to calculate i and $\mathbf{\Omega}$ using Equations 3.5 and 3.6. In the case of warped or broken disks, we use the local angular momentum vector $\vec{\mathbf{L}}(r)$ to transform each annulus separately.

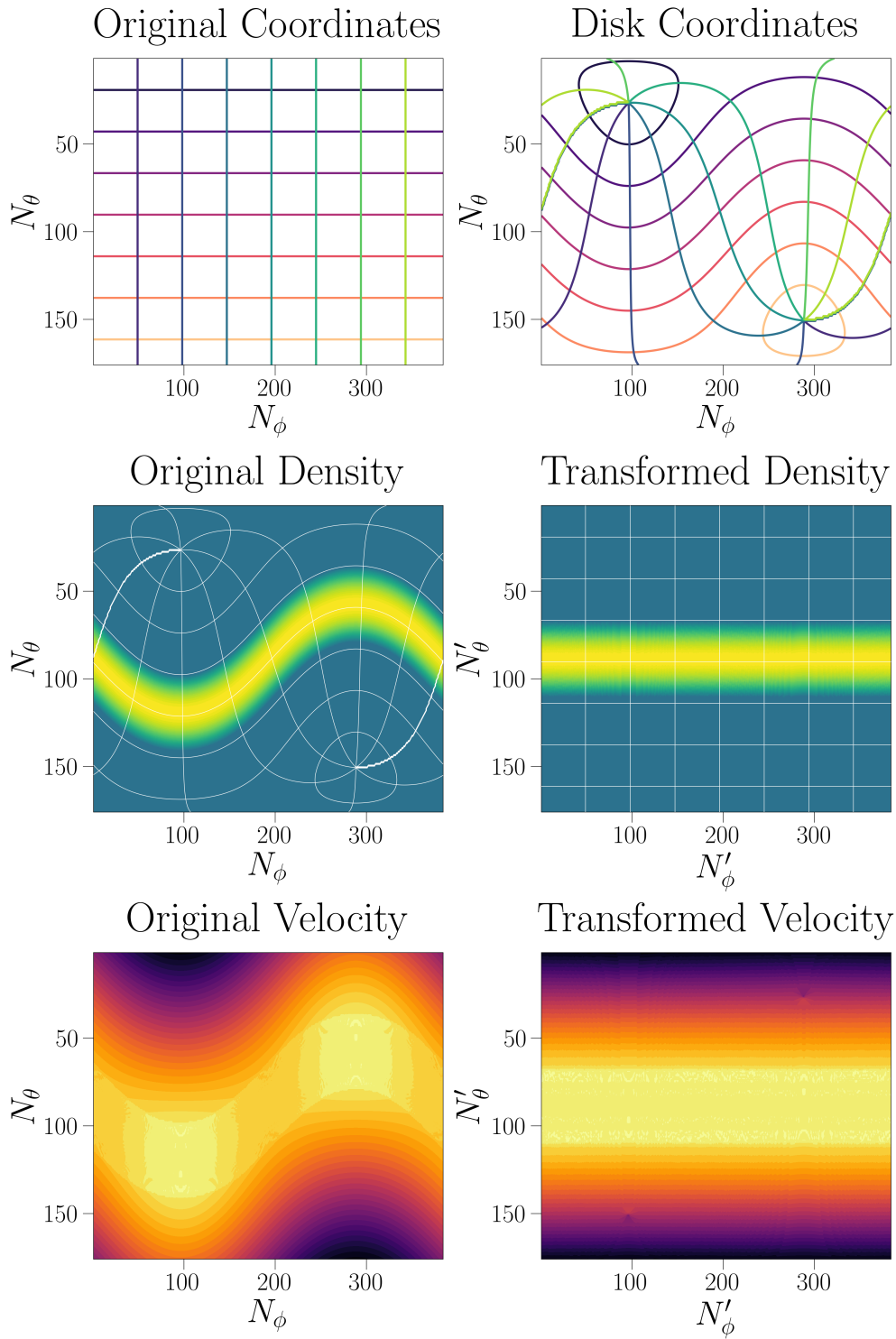


Figure A.1: Example of the coordinate transform using a 2D slice of the simulation data at $t = 0$. *Top Row:* Coordinate grid lines for the simulation and disk coordinates. *Middle Row:* Disk density in the simulation and disk coordinates. *Bottom Row:* Azimuthal velocity v_ϕ in the simulation and disk coordinates.

BIBLIOGRAPHY

- ALMA Partnership et al., 2015, *ApJ*, 808, L3
- Abod C. P., Chen C., Smallwood J., Rabago I., Martin R. G., Lubow S. H., 2022, *MNRAS*, 517, 732
- Aly H., Dehnen W., Nixon C., King A., 2015, *MNRAS*, 449, 65
- Andrews S. M., et al., 2018, *ApJ*, 869, L41
- Armstrong D., et al., 2013, *MNRAS*, 434, 3047
- Armstrong D. J., Osborn H. P., Brown D. J. A., Faedi F., Gómez Maqueo Chew Y., Martin D. V., Pollacco D., Udry S., 2014, *MNRAS*, 444, 1873
- Artymowicz P., Lubow S. H., 1996, *ApJ*, 467, L77
- Avenhaus H., Quanz S. P., Schmid H. M., Meyer M. R., Garufi A., Wolf S., Dominik C., 2014, *ApJ*, 781, 87
- Avenhaus H., et al., 2017, *AJ*, 154, 33
- Bae J., Hartmann L., Zhu Z., 2015, *ApJ*, 805, 15
- Bae J., Isella A., Zhu Z., Martin R., Okuzumi S., Suriano S., 2023, in Inutsuka S., Aikawa Y., Muto T., Tomida K., Tamura M., eds, *Astronomical Society of the Pacific Conference Series Vol. 534, Protostars and Planets VII.* p. 423 ([arXiv:2210.13314](https://arxiv.org/abs/2210.13314)), [doi:10.48550/arXiv.2210.13314](https://doi.org/10.48550/arXiv.2210.13314)
- Barrado Y Navascués D., 2006, *A&A*, 459, 511

Berger J. P., et al., 2011, A&A, 529, L1

Bi J., et al., 2020, ApJ, 895, L18

Boehler Y., et al., 2021, A&A, 650, A59

Brinch C., Jørgensen J. K., Hogerheijde M. R., Nelson R. P., Gressel O., 2016, ApJ, 830, L16

Burke B. F., 1957, AJ, 62, 90

Burrows C. J., Krist J. E., Stapelfeldt K. R., WFPC2 Investigation Definition Team 1995, in American Astronomical Society Meeting Abstracts. p. 32.05

Casassus S., 2016, Publ. Astron. Soc. Australia, 33, e013

Casassus S., et al., 2013, Nature, 493, 191

Casassus S., et al., 2015, ApJ, 811, 92

Chen C., Franchini A., Lubow S. H., Martin R. G., 2019, MNRAS, 490, 5634

Chen C., Lubow S. H., Martin R. G., 2020, MNRAS, 494, 4645

Chen C., Lubow S. H., Martin R. G., 2022, MNRAS, 510, 351

Childs A. C., Martin R. G., 2021, ApJ, 920, L8

Childs A. C., Martin R. G., 2022, ApJ, 927, L7

Childs H., et al., 2012, in , High Performance Visualization—Enabling Extreme-Scale Scientific Insight. pp 357–372

Cruz-Sáenz de Miera F., Kóspál Á., Ábrahám P., Liu H. B., Takami M., 2019, ApJ, 882, L4

Cuello N., Giuppone C. A., 2019, A&A, 628, A119

Czekala I., et al., 2017, ApJ, 851, 132

Debes J. H., et al., 2017, ApJ, 835, 205

Demianski M., Ivanov P. B., 1997, A&A, 324, 829

Doğan S., Nixon C. J., King A. R., Pringle J. E., 2018, MNRAS, 476, 1519

Doyle L. R., et al., 2011, Science, 333, 1602

Dullemond C. P., Kimmig C. N., Zanazzi J. J., 2022, MNRAS, 511, 2925

Duquennoy A., Mayor M., 1991, A&A, 248, 485

Dvorak R., 1986, A&A, 167, 379

Facchini S., Lodato G., Price D. J., 2013, MNRAS, 433, 2142

Facchini S., Juhász A., Lodato G., 2018, MNRAS, 473, 4459

Fang M., Sicilia-Aguilar A., Wilner D., Wang Y., Roccatagliata V., Fedele D., Wang J. Z.,
2017, A&A, 603, A132

Farago F., Laskar J., 2010, MNRAS, 401, 1189

Franchini A., Lubow S. H., Martin R. G., 2019, ApJ, 880, L18

Fromang S., Nelson R. P., 2005, MNRAS, 364, L81

Fu W., Li H., Lubow S., Li S., 2014, ApJ, 788, L41

Hammer M., Kratter K. M., Lin M.-K., 2017, MNRAS, 466, 3533

Hammer M., Lin M.-K., Kratter K. M., Pinilla P., 2021, MNRAS, 504, 3963

Harris C. R., et al., 2020, Nature, 585, 357

Holman M. J., Wiegert P. A., 1999, AJ, 117, 621

Hunter J. D., 2007, Computing in Science and Engineering, 9, 90

Izquierdo A. F., Facchini S., Rosotti G. P., van Dishoeck E. F., Testi L., 2022, ApJ, 928, 2

Juhász A., Facchini S., 2017, MNRAS, 466, 4053

Katz J. I., 1973, Nature Physical Science, 246, 87

Kennedy G. M., et al., 2019, Nature Astronomy, 3, 230

Keppler M., et al., 2020, A&A, 639, A62

Kerr F. J., Hindman J. V., Carpenter M. S., 1957, Nature, 180, 677

King A. R., Livio M., Lubow S. H., Pringle J. E., 2013, MNRAS, 431, 2655

Klahr H., Bodenheimer P., 2006, ApJ, 639, 432

Kouwenhoven M. B. N., Brown A. G. A., Portegies Zwart S. F., Kaper L., 2007, A&A, 474,

77

Kozai Y., 1962, AJ, 67, 591

Kraus S., et al., 2020, *Science*, 369, 1233

Kuznetsova A., Bae J., Hartmann L., Mac Low M.-M., 2022, *ApJ*, 928, 92

Larwood J. D., Nelson R. P., Papaloizou J. C. B., Terquem C., 1996, *MNRAS*, 282, 597

Lepp S., Martin R. G., Lubow S. H., 2023, *ApJ*, 943, L4

Li H., Finn J. M., Lovelace R. V. E., Colgate S. A., 2000, *ApJ*, 533, 1023

Lidov M. L., 1962, *Planet. Space Sci.*, 9, 719

Lin M.-K., 2012, *ApJ*, 754, 21

Lodato G., Price D. J., 2010, *MNRAS*, 405, 1212

Lodato G., Pringle J. E., 2007, *MNRAS*, 381, 1287

Lovelace R. V. E., Li H., Colgate S. A., Nelson A. F., 1999, *ApJ*, 513, 805

Lubow S. H., Martin R. G., 2018, *MNRAS*, 473, 3733

Lubow S. H., Ogilvie G. I., 2000, *ApJ*, 538, 326

Lubow S. H., Martin R. G., Nixon C., 2015, *ApJ*, 800, 96

Lynden-Bell D., Pringle J. E., 1974, *MNRAS*, 168, 603

Lyra W., Johansen A., Klahr H., Piskunov N., 2008, *A&A*, 491, L41

Marino S., Perez S., Casassus S., 2015, *ApJ*, 798, L44

Martin R. G., 2008, *MNRAS*, 387, 830

- Martin D. V., 2018, in Deeg H. J., Belmonte J. A., eds, , Handbook of Exoplanets. p. 156,
doi:10.1007/978-3-319-55333-7_156
- Martin D. V., Fabrycky D. C., 2021, AJ, 162, 84
- Martin R. G., Lubow S. H., 2017, ApJ, 835, L28
- Martin R. G., Lubow S. H., 2018, MNRAS, 479, 1297
- Martin R. G., Lubow S. H., 2019, MNRAS, 490, 1332
- Martin D. V., Triaud A. H. M. J., 2014, A&A, 570, A91
- Martin R. G., et al., 2019, ApJ, 875, 5
- Martin R. G., Lepp S., Lubow S. H., Kenworthy M. A., Kennedy G. M., Vallet D., 2022,
ApJ, 927, L26
- Mathieu R. D., Adams F. C., Latham D. W., 1991, AJ, 101, 2184
- Miranda R., Lai D., 2015, MNRAS, 452, 2396
- Miranda R., Muñoz D. J., Lai D., 2017, MNRAS, 466, 1170
- Miyoshi M., Moran J., Herrnstein J., Greenhill L., Nakai N., Diamond P., Inoue M., 1995,
Nature, 373, 127
- Monin J. L., Clarke C. J., Prato L., McCabe C., 2007, in Reipurth B., Jewitt D., Keil K., eds,
Protostars and Planets V. p. 395 (arXiv:astro-ph/0604031), doi:10.48550/arXiv.astro-
ph/0604031

Montesinos M., Perez S., Casassus S., Marino S., Cuadra J., Christiaens V., 2016, ApJ, 823, L8

Muñoz D. J., Lai D., 2016, ApJ, 827, 43

Nealon R., Price D. J., Nixon C. J., 2015, MNRAS, 448, 1526

Nealon R., Ragusa E., Gerosa D., Rosotti G., Barbieri R., 2022, MNRAS, 509, 5608

Nixon C., King A., 2016, in Haardt F., Gorini V., Moschella U., Treves A., Colpi M., eds, , Vol. 905, Lecture Notes in Physics, Berlin Springer Verlag. p. 45, doi:10.1007/978-3-319-19416-5_2

Nixon C., King A., Price D., Frank J., 2012, ApJ, 757, L24

Nixon C., King A., Price D., 2013, MNRAS, 434, 1946

Offner S. S. R., Moe M., Kratter K. M., Sadavoy S. I., Jensen E. L. N., Tobin J. J., 2023, in Inutsuka S., Aikawa Y., Muto T., Tomida K., Tamura M., eds, Astronomical Society of the Pacific Conference Series Vol. 534, Protostars and Planets VII. p. 275 (arXiv:2203.10066), doi:10.48550/arXiv.2203.10066

Ogilvie G. I., 1999, MNRAS, 304, 557

Owen J. E., Kollmeier J. A., 2017, MNRAS, 467, 3379

Papaloizou J. C. B., Lin D. N. C., 1995, ApJ, 438, 841

Papaloizou J. C. B., Pringle J. E., 1983, MNRAS, 202, 1181

Petterson J. A., Rothschild R. E., Gruber D. E., 1991, ApJ, 378, 696

Pinte C., Dent W. R. F., Ménard F., Hales A., Hill T., Cortes P., de Gregorio-Monsalvo I.,
2016, ApJ, 816, 25

Price D. J., et al., 2018, MNRAS, 477, 1270

Pringle J. E., 1981, ARA&A, 19, 137

Pringle J. E., 1992, MNRAS, 258, 811

Quarles B., Satyal S., Kostov V., Kaib N., Haghighipour N., 2018, ApJ, 856, 150

Ragusa E., Dipierro G., Lodato G., Laibe G., Price D. J., 2017, MNRAS, 464, 1449

Ragusa E., Alexander R., Calcino J., Hirsh K., Price D. J., 2020, MNRAS, 499, 3362

Raj A., Nixon C. J., Doğan S., 2021, ApJ, 909, 81

Scott D. M., Leahy D. A., Wilson R. B., 2000, ApJ, 539, 392

Shakura N. I., Sunyaev R. A., 1973, A&A, 24, 337

Shi J.-M., Krolik J. H., Lubow S. H., Hawley J. F., 2012, ApJ, 749, 118

Shu F. H., Cuzzi J. N., Lissauer J. J., 1983, Icarus, 53, 185

Simon M., Guilloteau S., 1992, ApJ, 397, L47

Smallwood J. L., Lubow S. H., Franchini A., Martin R. G., 2019, MNRAS, 486, 2919

Smallwood J. L., Nealon R., Chen C., Martin R. G., Bi J., Dong R., Pinte C., 2021, MNRAS,
508, 392

Smallwood J. L., Lubow S. H., Martin R. G., 2022, MNRAS, 514, 1249

Stone J. M., Gardiner T., 2009, *New Astron.*, 14, 139

Stone J. M., Tomida K., White C. J., Felker K. G., 2020, *ApJS*, 249, 4

Takeuchi T., Lin D. N. C., 2002, *ApJ*, 581, 1344

Teague R., Bae J., Bergin E. A., Birnstiel T., Foreman-Mackey D., 2018, *ApJ*, 860, L12

Teague R., Bae J., Bergin E. A., 2019, *Nature*, 574, 378

Villeneuve M., et al., 2022, *ApJ*, 930, 11

Weidenschilling S. J., 1977, *MNRAS*, 180, 57

Welsh W. F., Orosz J. A., Carter J. A., Fabrycky D. C., 2014, in Haghhighipour N., ed.,
Vol. 293, *Formation, Detection, and Characterization of Extrasolar Habitable Planets*. pp
125–132 ([arXiv:1308.6328](https://arxiv.org/abs/1308.6328)), doi:10.1017/S1743921313012684

Young A. K., Stevenson S., Nixon C. J., Rice K., 2023, *MNRAS*, 525, 2616

Zanazzi J. J., Lai D., 2018, *MNRAS*, 473, 603

Zhu Z., 2019, *MNRAS*, 483, 4221

Zhu Z., Stone J. M., 2014, *ApJ*, 795, 53

Zhu Z., Stone J. M., Rafikov R. R., Bai X.-n., 2014, *ApJ*, 785, 122

Zhu Z., Dong R., Stone J. M., Rafikov R. R., 2015, *ApJ*, 813, 88

Zúñiga-Fernández S., et al., 2021, *A&A*, 655, A15

de Val-Borro M., Artymowicz P., D’Angelo G., Peplinski A., 2007, *A&A*, 471, 1043

van der Marel N., et al., 2013, *Science*, 340, 1199

von Zeipel H., 1910, *Astronomische Nachrichten*, 183, 345

CURRICULUM VITAE

Graduate College
University of Nevada, Las Vegas

Ian Rabago

Department of Physics and Astronomy
University of Nevada, Las Vegas
Las Vegas, NV 89154

Email: rabagoian@gmail.com
Personal Website

EDUCATION

University of Nevada, Las Vegas

2020	Masters of Science, Astronomy
2018	Bachelor of Science, Physics Concentration in Computational Physics Bachelor of Science, Mathematics

AWARDS

2020	Nevada NASA Space Grant Consortium Fellowship
2018	UNLV Image of Research Contest Winner, Graduate Student Category

WORK EXPERIENCE

2018-Present	PhD Student [Advisor: Zhaohuan Zhu] Computational astrophysics, protoplanetary disk dynamics Python, C++ ATHENA++ grid-based hydrodynamics code
2016-2018	Undergraduate research [Advisor: Jason Steffen] N-body dynamical simulations Python, REBOUND N-body code
2013-2018	Mathematics instructor at Mathnasium of Green Valley Tutoring K-12 students in mathematics

OTHER EXPERIENCE

SCIENCE OUTREACH

Astronomy on Tap, Las Vegas - astronomy-themed bar trivia night

Scorekeeper and Question Writer, 2019-Present

Science Olympiad - Science competition for middle and high school students

2022 Event supervisor and judge, Astronomy Division C

Beal Bank Science Fair - Science fair for K-12 students

Judge, 2022-2023

SCIENCE-INSPIRED ARTWORK

Inquiry: The Art of Scientific Discovery - Science-themed art gallery at UNLV

Artwork showcased during exhibits in 2017, 2018, and 2022

PUBLICATIONS

Ian Rabago, Zhaohuan Zhu, Rebecca Martin, and Stephen Lubow. "Warps and Breaks in Protoplanetary Disks". Submitted to MNRAS.

DOI:10.48550/arXiv.2310.00459 arxiv:2310.00459

Ian Rabago, Zhaohuan Zhu, Rebecca Martin, and Stephen Lubow. "Grid-Based Simulations of Polar Aligned Circumbinary Disks: Polar Alignment and Vortex Formation". MNRAS, 520, 2, January 2023.

DOI:10.1093/mnras/stad242 arxiv:2301.07796

Charles Abod, Chen Cheng, Jeremy Smallwood, **Ian Rabago**, Rebecca Martin, and Stephen Lubow. "Polar alignment of a massive retrograde circumbinary disc around an eccentric binary". MNRAS, 517,1, November 2022.

DOI:10.1093/mnras/stac2601 arxiv:2209.14466

Luca Ricci, Ben Burrill, **Ian Rabago**, and Zhaohuan Zhu. "NGVLA Memo 101: Mapping the Gas Density and Kinematic Structures due to Embedded Protoplanets in Young Disks with the Next Generation Very Large Array". September 2022.

Ian Rabago and Zhaohuan Zhu. "Constraining Protoplanetary Disk Accretion and Young Planets Using ALMA Kinematic Observations". MNRAS, 502,4, April 2021

DOI:10.1093/mnras/stab447 arxiv:2102.03007

Ian Rabago and Jason Steffen. "Survivability of Moon Systems Around Ejected Gas Giants". MNRAS, 489,2, October 2019.

DOI:10.1093/mnras/sty2552 arxiv:1809.05639

CONFERENCE PRESENTATIONS

Dynamics of Circumbinary Disks [Presentation]
American Astronomical Society #243. New Orleans, LA. January 2024

Dynamics of Circumbinary Disks [Presentation]
TCAN Disk Hydro & Planet Formation Workshop. Tuscon, AZ. November 2023

Warps and Breaks in Protoplanetary Disks. [Poster]
Gordon Research Conference. South Hadley, MA. June 2023.

Dynamics of Circumbinary Disks. [Presentation]
Athena++ Conference. New York, NY. May 2023.

Warps and Breaks in Protoplanetary Disks. [Poster]
Protostars and Planets VII. Tokyo, Japan. April 2023.

Polar Alignment and Vortices in Circumbinary Disks. [Poster]
Exoplanets IV. Las Vegas, NV. May 2022

Grid-Based Simulations of Polar Aligned Circumbinary Disks. [Presentation]
New paradigms for Radiatively Efficient Accretion Disks Workshop. New York, NY, December 2021

Constraining Protoplanetary Disk Accretion and Young Planets Using ALMA Kinematic Observations. [Presentation]
Five Years After HL Tau: A New Era in Planet Formation. Online conference, December 2020

Grid-Based Simulations of Tilted Circumbinary Disks. [Poster]
New Horizons in Planetary Systems. Victoria, BC. May 2019

The Survivability of Moons Around an Escaping Planet. [Poster]
American Astronomical Society #231. Washington DC, January 2018